Research Square

Preprints are preliminary reports that have not undergone peer review.
They should not be considered conclusive, used to inform clinical practice,
or referenced by the media as validated information.

A photodoped monoclinic doorway governs the ultrafast transition in VO_2

Chong-Yu ruan

ruan@pa.msu.edu

Michigan State University

Xiaoyi Sun

Michigan State University

Sachin Sharma

Michigan State University

Tri Duc Nguyen

Michign State University

Ian Gonzalez-Afanador

Michigan State University

Nelson Sepulveda

Michigan State University https://orcid.org/0000-0002-9676-8529

Kai Sun

University of Michigan https://orcid.org/0000-0003-1745-9136

Physical Sciences - Article

Keywords:

Posted Date: November 20th, 2026

DOI: https://doi.org/10.21203/rs.3.rs-11777053/v1

License: This work is licensed under a Creative Commons Attribution 4.0 International License.
Read Full License

Additional Declarations: There is **NO** Competing Interest.

A photodoped monoclinic doorway governs the ultrafast transition in VO_2

Xiaoyi Sun[1], Sachin Sharma[1], Tri Duc Nguyen[1], Ian Gonzalez-Afanador[2], Nelson Alancastro Sepúlveda[2], Kai Sun[3], Chong-Yu Ruan[1*]

[1]Department of Physics and Astronomy, Michigan State University, East Lansing, MI, 48824, USA
[2]Department of Electrical and Computer Engineering, Michigan State University, East Lansing, MI, 48824, USA
[3]Department of Materials Science and Engineering, University of Michigan, Ann Arbor, MI, 48109, USA
*Corresponding author: Chong-Yu Ruan (ruanc@msu.edu)

The insulator–metal transition in VO_2 is a paradigm of coupled electronic and structural phase change, yet its photoinduced pathway has resisted a unified microscopic description. Electronic gap collapse, monoclinic metallicity, lattice disorder and thermal switching have each been observed[1–4], but whether they constitute competing mechanisms or successive stages of one transformation has remained unresolved. Here we show that the photoinduced transition proceeds through a hidden monoclinic intermediate, with electronic initiation and structural conversion governed by distinct physical thresholds. Simultaneous sub-50-fs electron diffraction and optical spectroscopy, combined with physics-informed structural inversion and first-principles optical calculations, reveal an electronically active intermediate retaining 63% of the insulating phase's V–V dimerization. A photocarrier-associated threshold opens this pathway, accompanied by pronounced slowing of the optical response near onset, while polarization anisotropy reveals carrier contributions beyond those of the reconstructed lattice. The intermediate converts into a rutile-like average structure whose optical response continues to mature, consistent with transient local V–V distortions lacking interchain registry. A second, thermally governed threshold determines the converted volume and crystallographic texture through energy redistribution between grains. These findings establish that electronic instability and structural phase conversion are not a single event: photocarriers open a transient monoclinic pathway, while lattice reorganization and collective energy redistribution govern the emergence and extent of metallic functionality.

A first-order phase transition is defined by its equilibrium endpoints; a photoinduced transition is governed by the pathway between them. This distinction is fundamental in correlated solids, where an electronic instability may emerge before the crystal reorganizes, and where the structure of the newly formed phase need not immediately possess its equilibrium functionality. For correlated quantum-material electronics—from threshold switches and neuromorphic memory to reconfigurable photonics—controlling the speed, energy cost and persistence of a transition demands understanding not only its endpoints but also the microscopic cascade that creates its function[5,6]. VO_2 exemplifies the problem. Its sharp equilibrium transformation links the monoclinic, V–V-dimerized insulator to a rutile metal, making it a canonical setting for the interplay of

electronic correlation and lattice symmetry[7–11]. Under femtosecond excitation, however, the material need not follow the equilibrium route. Our central finding is that the optical switch is organized by a transient, partially dimerized doorway through which electronic destabilization is converted into structural transformation, while a distinct thermal threshold determines the volume and texture of the product.

The history of ultrafast VO_2 reveals why the doorway matters. Photocarrier-driven gap collapse established that metallic electronic response can be initiated on a timescale faster than structural equilibration[1]. Ultrafast diffraction identified a monoclinic metal-like state and a stepwise lattice response[2,12,13], while coherent phonon measurements and ultrafast disordering demonstrated that lattice dynamics and V–V correlations remain central[3,14–16]. Separate studies pointed to distinct electronic and structural thresholds[17,18], whereas thermal analyses emphasized deposited energy[4]. The deeper implication from these diverse discoveries is that the photoinduced transition cannot be identified solely with the disappearance of an insulating reflection, the arrival of optical metallicity or the eventual rutile lattice: each may report a different event along one evolving trajectory.

The unresolved physical question is therefore not whether the transition is *Mott or Peierls*, or whether heat contributes, but **how these distinct mechanisms are sequenced and coupled**. Does photodoping first create an electronically distinct state without erasing monoclinic order? Is the rutile-like product born with the short-range coherence and optical response of equilibrium rutile, or does it mature after its Bragg structure forms? Can the onset of metallicity and the completion of phase conversion be controlled separately? Answering these questions requires tracking the electronic function and the atomic configuration under the same excitation, and determining whether their independently measured trajectories can arise from a single microscopic account.

To establish when an evolving atomic arrangement acquires electronic functionality, we combine high-brightness, sub-50-fs ultrafast electron diffraction[19–21] with synchronized optical pump–probe spectroscopy on the same sample film and clock, extending across 21 reflections, a broad fluence range and polarization-resolved electronic readout (Fig. 1). This temporal and experimental co-registration anchors the unfolding optical response to a directly measured structural trajectory rather than comparing separate experiments after the fact. Rather than assigning a structure independently to every delay, physics-guided inversion[22,23] of the diffraction manifold couples phase populations to causal kinetics and dynamical electron scattering[24], while subsequent refinement reconstructs per-phase atomic coordinates. Crucially, DFT+U calculations on these unrelaxed reconstructed structures predict optical functionality, so that the measured electronic response can challenge the structural assignment. When the average structure alone does not account for optical

anisotropy or delayed transmission, explicit carrier and local-disorder models are tested rather than absorbed into unconstrained reflection amplitudes. The methodological advance is decisive because it exposes the physics of a transforming state that neither structural nor optical observations identify independently.

We find a sequence of physically differentiated stages. Photodoping opens a nonthermal threshold near 4.4 mJ cm^{-2}, producing an optically active monoclinic intermediate that preserves substantial V–V pairing; the transformation then proceeds toward a rutile-like product with evolving local order, before intergrain heat redistribution fixes the final transformed volume and crystallographic texture near a second threshold of approximately 7.1 mJ cm^{-2}. This pathway turns previously disparate observations into a mechanistic sequence with distinct origins, timescales and control parameters. It establishes how a correlated transition can be electronically initiated, structurally mediated and thermally completed, without reducing any one of those processes to another.

Results

A transient monoclinic doorway separates electronic and structural transitions

The transformation first separates into structurally distinct stages: monoclinic superlattice order weakens, a partially dimerized intermediate accumulates and a rutile-like product subsequently emerges (Fig. 2a). The 17 fitted reflections differ in onset, amplitude and recovery. The M1 superlattice reflections, such as $(30\bar{2})$ and $(31\bar{3})$, which report V–V pairing and zigzag, vanish at 8.40 and 11.22 mJ cm^{-2}, decline only partially at 6.90 mJ cm^{-2} and remain near their pre-pump values at 4.29 mJ cm^{-2} (all fluences, Extended Data Fig. 1). The transmission change recorded simultaneously on the same film cannot be mapped onto any single reflection and reverses sign between 4.29 and 4.52 mJ cm^{-2} (Fig. 3a). Structural and electronic observables are therefore coupled but not redundant, a first indication that intermediate states carry distinct optical and diffraction signatures.

The doorway is embedded in a coherent lattice response shared by electron diffraction and optical spectroscopy, not in an electronically isolated switching channel (Fig. 2b). A single model of three damped A_g oscillators reproduces six oxygen-displacement channels from diffraction and five polarization-resolved optical traces at 8.0 mJ cm^{-2} (441 points, reduced χ^2 0.93), with frequencies and damping shared across channels and only amplitudes and phases free per trace (Methods). The oxygen-cage breathing (4.43 THz), torsional (5.67 THz) and V–V chain (7.46 THz) modes are thus common to both probes, the chain mode carrying 65%

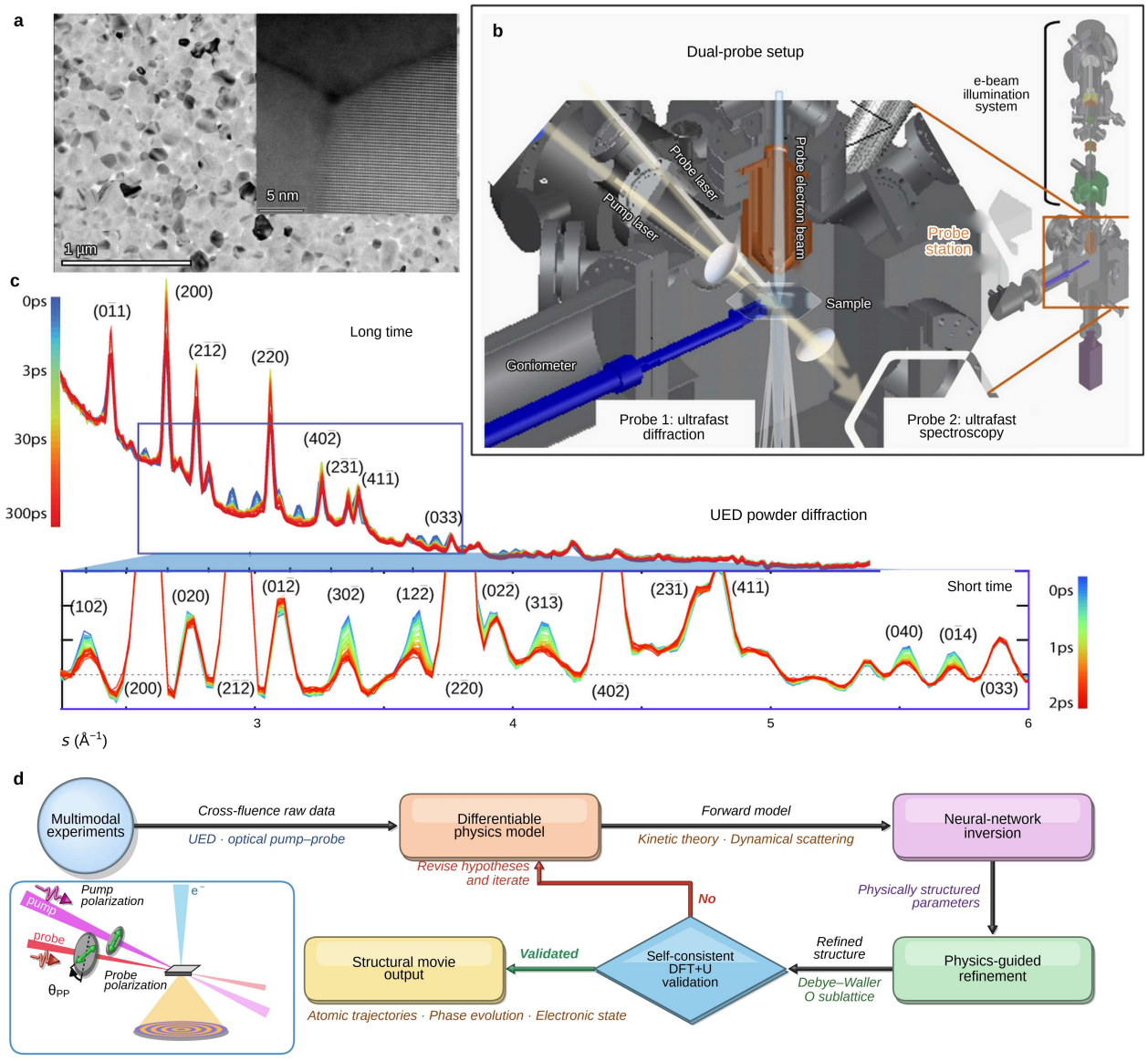


Fig. 1 | Multimodal measurements and physics-informed inversion reconstruct the nonequilibrium structure–function pathway. a, Scanning transmission electron microscopy (STEM) of the VO_2 film on a 9-nm SiN_x membrane: randomly oriented grains 40–90 nm across (scale bar, 1 µm). Inset, atomic-resolution image of a grain-boundary junction; each grain is single-crystalline up to the boundary (scale bar, 5 nm). **b**, Dual-probe geometry in UEM-1. A 1.55-eV pump pulse excites the film; an electron pulse (UED) and an 800-nm optical pulse (transmission, OPP) probe it under the same excitation on one time axis. Inset, pump and probe polarizations and their angle θ_{PP}. **c**, Radially averaged UED patterns against the scattering vector s at 0–300 ps (top) and, for the boxed window, at 0–2 ps (bottom; reflections labeled by M1 indices), at about 8.0 mJ cm^{-2}; by 2 ps the $(30\bar{2})$ and $(31\bar{3})$ superlattice peaks fall to 0.4–0.5 of their pre-pump height. The M1 superlattice reflections report the V–V dimerization and twist. **d**, Inversion workflow. A neural network trained on simulations of a differentiable forward model (four-species kinetics of the monoclinic insulator M1, the polaronic metal pM, the rutile-like phase R* and a defect channel D without Bragg signature; dynamical electron scattering) inverts the diffraction data of all fluences into phase fractions and structures, which a physics-guided refinement adjusts frame by frame (Debye–Waller factors, oxygen sublattice). DFT+U calculations of each refined structure predict the OPP data; a failed prediction revises the hypotheses of the model and the loop repeats. Inset, the polarization geometry: pump and optical-probe pulses with their polarizations (discs) and the angle θ_{PP} between them, the electron probe (e^-), the sample and the diffraction cone on the detector.

of the diffracted vibrational energy and 64% of the coherent optical signal. Their weak angular dependence has the sign of photoselected softening (Extended Data Fig. 2).

At atomic resolution, the hidden doorway is neither intact M1 nor nascent rutile: it is a partially dedimerized, partially detwisted monoclinic structure with a finite lifetime and a distinct electronic response (Fig. 2c). At 8.40 mJ cm^{-2} the dimerization Δ(V–V) falls from 0.600 Å in the monoclinic insulator (M1) to 0.376 Å in the doorway state (pM, 0.56 ps) and to 0.09–0.10 Å in the rutile-like product (R*) at 2–15 ps, while the V–V–V chain angle straightens from 166.1° to 173.7° and then to 177.7–179.7°; pM thus retains 63% of the dimerization and 45% of the twist. This collapse exceeds the structural precision by more than an order of magnitude (±0.007 Å in Δ(V–V) and ±0.2° where R* is static; ≤ 0.058 Å between independent refinement passes). The pM vanadium motif was refined freely in earlier iterations of the inversion and converged to the values used here, while the R* vanadium coordinates, the oxygen displacement, the lattice and the Debye–Waller factors are refined at every delay (Methods); the photodoped carriers identified below act on the M1 lattice in precisely the way this partially dedimerized and detwisted motif implies.

The rutile-like product acquires its optical identity after much of its Bragg conversion is complete, exposing a second stage of the transformation invisible to average crystallography. At 8.40 mJ cm^{-2}, 44% of the film has left M1 by 0.3 ps, pM peaks at a fraction of 0.66 at 1.2 ps and R* overtakes it at 3.0 ps, reaching 90% of its late value by 9 ps (Fig. 4a). The 60° transmission, by contrast, has attained only 59% of its plateau at 9 ps and 80% at 30 ps. The internal state of the converted volume is therefore resolved only when the refined structures are confronted with the optical response through first-principles calculations, as developed below.

Photocarriers initiate the transition at a distinct onset threshold

Metallicity is switched on above a nonthermal threshold, F_c = 4.40 mJ cm^{-2}, at which the transition exhibits critical slowing down (Fig. 3a; Fig. 4b). The long-time optical order parameter changes sign between 4.29 and 4.52 mJ cm^{-2} (from −0.0241 ± 0.0008 to +0.0208 ± 0.0008), and threshold fits to the diffraction and optical data without a kinetic model give 4.24 ± 0.22 and 4.45 ± 0.30 mJ cm^{-2}. On approaching F_c from above, the half-rise time of the measured ΔT/T lengthens from 0.63 ps at 13.64 mJ cm^{-2} to 5.6 ps at 8.40 mJ cm^{-2} and 157 ps at 5.00 mJ cm^{-2}, a 249-fold slowing; at 4.52 mJ cm^{-2} no visible rise exceeds 3% within 3 ns (maximum ΔT/T 0.023), and at 4.29 mJ cm^{-2} the late signal is negative. This identification rests on the measured optical timescale; the corresponding structural timescale, the time for R* to reach 1% of the film (24 fs to 140 ps), follows the same trend but is shaped by the critical gate of the kinetic prior (Methods).

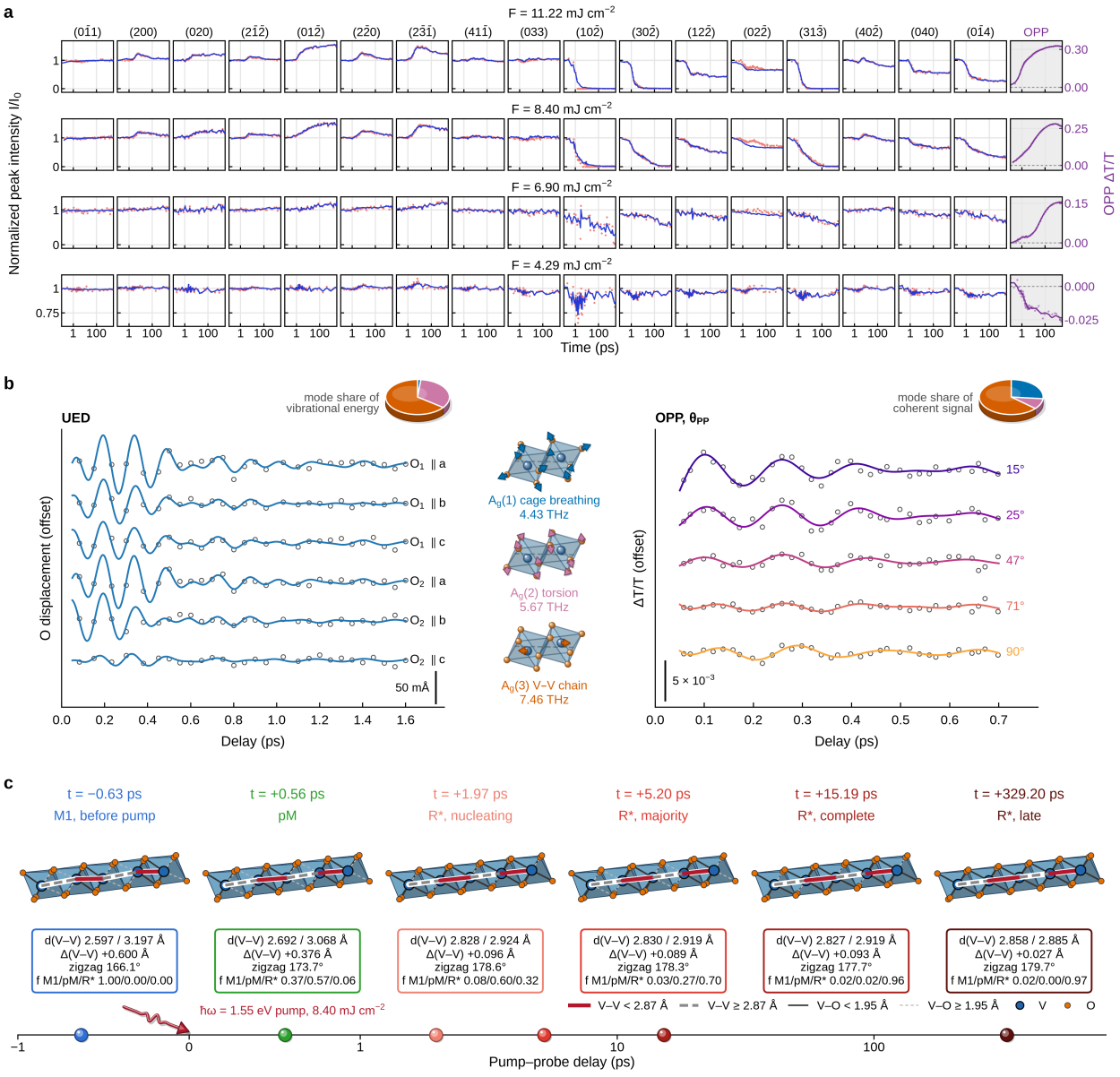

a
F = 11.22 mJ cm−2
F = 8.40 mJ cm−2
F = 6.90 mJ cm−2
F = 4.29 mJ cm−2
(0$\bar{1}$1)
(200)
(020)
(2$\bar{1}\bar{2}$)
(01$\bar{2}$)
(2$\bar{2}$0)
(2$\bar{3}\bar{1}$)
(41$\bar{1}$)
(033)
(10$\bar{2}$)
(30$\bar{2}$)
(12$\bar{2}$)
(02$\bar{2}$)
(31$\bar{3}$)
(40$\bar{2}$)
(040)
(0$\bar{1}$4)
OPP
Normalized peak intensity I/I0
OPP ΔT/T
Time (ps)
b
UED
mode share of vibrational energy
O displacement (offset)
O1 ‖ a
O1 ‖ b
O1 ‖ c
O2 ‖ a
O2 ‖ b
O2 ‖ c
50 mÅ
Delay (ps)
Ag(1) cage breathing 4.43 THz
Ag(2) torsion 5.67 THz
Ag(3) V–V chain 7.46 THz
OPP, θPP
mode share of coherent signal
ΔT/T (offset)
15°
25°
47°
71°
90°
5 × 10−3
Delay (ps)
c
t = −0.63 ps
M1, before pump
t = +0.56 ps
pM
t = +1.97 ps
R*, nucleating
t = +5.20 ps
R*, majority
t = +15.19 ps
R*, complete
t = +329.20 ps
R*, late
d(V–V) 2.597 / 3.197 Å
Δ(V–V) +0.600 Å
zigzag 166.1°
f M1/pM/R* 1.00/0.00/0.00
d(V–V) 2.692 / 3.068 Å
Δ(V–V) +0.376 Å
zigzag 173.7°
f M1/pM/R* 0.37/0.57/0.06
d(V–V) 2.828 / 2.924 Å
Δ(V–V) +0.096 Å
zigzag 178.6°
f M1/pM/R* 0.08/0.60/0.32
d(V–V) 2.830 / 2.919 Å
Δ(V–V) +0.089 Å
zigzag 178.3°
f M1/pM/R* 0.03/0.27/0.70
d(V–V) 2.827 / 2.919 Å
Δ(V–V) +0.093 Å
zigzag 177.7°
f M1/pM/R* 0.02/0.02/0.96
d(V–V) 2.858 / 2.885 Å
Δ(V–V) +0.027 Å
zigzag 179.7°
f M1/pM/R* 0.02/0.00/0.97
ħω = 1.55 eV pump, 8.40 mJ cm−2
V–V < 2.87 Å
V–V ≥ 2.87 Å
V–O < 1.95 Å
V–O ≥ 1.95 Å
V
O
Pump–probe delay (ps)

Fig. 2 |Atomic reconstruction reveals a partially dimerized monoclinic doorway to the metallic phase. a, Normalized intensity I/I_0 of 17 Bragg reflections (M1 indices) at 11.22, 8.40, 6.90 and 4.29 mJ cm^{-2} (rows; all fluences in Extended Data Fig. 1). Red dots, measured; blue lines, computed from the refined phase fractions, structures and Debye–Waller factors with dynamical scattering. Last column (gray, right axis), ΔT/T of the same film, measured (light purple) and decomposed on the phase fractions (purple; Fig. 3a). **b**, Coherent A_g phonons at 8.0 mJ cm^{-2} from one joint fit of both probes. Left, UED displacements of the oxygen sites O1 and O2 along the M1 axes a, b and c (scale bar, 50 mÅ); right, OPP ΔT/T at θ_{PP} = 15, 25, 47, 71 and 90° (scale bar, 5 × 10^{-3}). Circles, data after removal of a polynomial background; lines, joint fit convolved with the response of each probe (Methods). Center, the three modes drawn on two edge-sharing VO_6 cages of the refined M1 (arrows, displacement pattern, not to scale) with their fitted frequencies; pies, share of each mode in the diffracted vibrational energy and in the coherent optical signal. **c**, One V chain of five edge-sharing VO_6 octahedra in the refined structure of the dominant phase at 8.40 mJ cm^{-2}: M1 at −0.63 ps, pM at 0.56 ps and R* at 1.97, 5.20, 15.19 and 329.20 ps. V–V bonds shorter than 2.87 Å red, longer gray dashed; V–O bonds shorter than 1.95 Å dark, longer light dashed. Boxes, short and long V–V distances, their difference Δ(V–V), the V–V–V angle and the phase fractions; bottom, the six delays on the pump–probe axis, with the pump pulse at time zero. DFT+U response in Extended Data Fig. 4.

The threshold is set by carrier density rather than by deposited heat. Using the measured optical differential transmittance (absorbed fraction 0.28–0.39; Methods), the photo-hole density at F_c is 0.6–1.3 × 10^{21} cm^{-3} (0.02–0.04 holes per V), coincident with the critical absorbed-photon density previously identified in such films[18] and with the density at which photocarrier doping collapses the gap[1], and comparable to a Mott criterion under electronic screening[25]. The heat deposited at F_c would warm the equilibrated film to 341–346 K, within its broadened thermal transition, yet the late R* fraction remains 0.000, 0.0006 and 0.019 at 4.29, 4.52 and 5.00 mJ cm^{-2}. Below F_c heat does not open the pathway; above it, the pathway runs through pM.

Electronic metallicity precedes structural conversion: the converted volume is optically metallic while its lattice is still monoclinic (Fig. 3b). Mapping each phase onto its optical metallicity, the absorption change relative to cold M1 assigned by a per-fluence decomposition of ΔT/T, shows the converted volume more metallic than M1 at every fluence above F_c from the first picosecond, when pM dominates. The DFT+U response of the refined structures identifies the origin of this contrast. At the probe, pM retains nearly all of the M1 absorption along the chains ($\varepsilon_{2\parallel}$ 11.2 versus 12.5) but loses half of it across them ($\varepsilon_{2\perp}$ 2.8 versus 5.4), whereas R* loses both (1.3 and 1.6). The monoclinic metal inferred previously from separate diffraction and optical experiments[2,12] is thus observed here in a single measurement and located on the transition pathway.

A second, thermal threshold determines how much of the film converts. The late R* fraction (1–3 ns), which follows the measured superlattice intensities, rises from 0.02 at 5.00 to 0.97 at 8.40 mJ cm^{-2} and crosses one half at F_{50} = 7.1 mJ cm^{-2} (7.07–7.17; Fig. 4b and Extended Data Fig. 5a). The polarization-resolved optics, analyzed without diffraction input, independently require a per-grain energy threshold e_c = 7.15 ± 0.08 mJ cm^{-2} (Fig. 3e), within 1% of F_{50}. The two thresholds therefore separate the initiation of the pathway from

its completion.

Rutile-like structural order precedes optical maturation

The optical lag arises because R* forms with local M1-like order but without phase coherence between chains, a state invisible to Bragg diffraction (Fig. 3c; Extended Data Fig. 6). ΔT/T computed from the DFT+U dielectric tensors of the refined structures, weighted by the refined fractions and mixed by effective-medium theory with one scale factor per film (Methods), reproduces the early rise but not the slow approach to the plateau: the R* contribution saturates only at ~100 ps, an order of magnitude after the R* fraction. Supercells of 96 atoms built on the refined R*, in which each chain carries a fraction λ of the M1 pairing and zigzag with signs uncorrelated between chains, return the refined R* intensity in every Bragg reflection and remain within its measured Debye–Waller excess, yet raise the absorption along c_R ($\varepsilon_{2\parallel}$ 15.7 at λ = 0.85, against 2.3 for ordered R*; raw DFT units). With λ decaying as a stretched exponential with a 50-ps time constant (0.85 at 3.7 ps, 0.5 at 30 ps and 0.25 at 80 ps) and newly converted R* acquiring this response within 2 ps, the computed transient reproduces the 60° transmission at 8.40 mJ cm^{-2} over 3.3 ns (R^2 = 0.988) and the first 2.5 ps at 8.0 mJ cm^{-2} on a second film (R^2 = 0.825, a window that also carries the coherent phonons absent from the model).

R* is therefore born one-dimensional—rutile on Bragg average but without interchain phase order—and acquires three-dimensional coherence only over tens of picoseconds. This assignment reconciles the stepwise pathway resolved by Bragg diffraction[13] with the ultrafast dimer disordering observed in total scattering[3,16]: the disorder is interchain and transient, and it orders into coherent R*. The near-unity Avrami exponent of the conversion kinetics[26,27] (0.95–1.2; Methods) is consistent with one-dimensional growth, and diffuse scattering perpendicular to c_R at 1–10 ps offers a direct test.

Photocarriers impart distinct optical functionality to the monoclinic doorway

The early polar anisotropy cannot be generated by any refined lattice configuration and instead requires the photodoped carriers (Fig. 3d; Extended Data Fig. 7). Because the anisotropy α in $\Delta T/T \propto \cos^2\theta + \alpha \sin^2\theta$ is independent of the optical scale, it provides a scale-free test of the structures. Relative to cold M1, the refined pM bleaches more across the chains than along them (at 1 ps, ε_2 17.2 along and 4.4 across, against 19.2 and 8.1), whereas the measured α at 1 ps requires the opposite, 13.9 along and 6.0 across. Every refined

structure—photoexcited M1, pM and R* at all delays, and R* with its local distortion—falls on a single trend from M1 to R* on which structures absorbing 13.9 along the chains absorb only 3.8–4.0 across them.

A single carrier term combining a hole bleach along the chains with an electron absorption across them resolves this deficit. Photoexcitation transfers electrons from the $d_{\parallel}$ bonding states of the V–V dimers to π*[7]; the resulting holes bleach the dimer transition polarized along c_{R}, while π* electrons absorb across the chains. Added to pM and to the R* converted from it within ~10 ps, with along-to-across strengths in the ratio −5 : +1 and no lifetime of its own, this term turns the pM response to the required shape and brings the polar data at six fluences into agreement with the model (χ^2/n = 2.41; 219 values of α at 0.5–800 ps). Between 0.5 and 2 ps pM carries 69–90% of both the isotropic and the anisotropic signal, so the early polar state is a direct measurement of the doorway. pM is therefore a polaronic metal in the operational sense that its optical response is carried by photodoped charges coupled to a partially dedimerized lattice.

Charged-supercell calculations show that the bleach along the chains is a cooperative, one-dimensional property of condensed holes. In 32-V DFT+U cells with frozen geometries, isolated or dispersed holes bleach predominantly across the chains (per hole, $\Delta\varepsilon_{2\parallel}/\Delta\varepsilon_{2\perp}$ = +0.011/−0.087 for an isolated hole), whereas holes on a fully unpaired chain bleach along it (−0.237/−0.043), more strongly when two such chains are adjacent (−0.327/−0.050); the adjacent-chain arrangement is also lower in energy, by 0.44 eV per cell, through the lattice. These calculations reproduce the sign, polarization and cooperativity of the required term but supply only 9–26% of its amplitude and do not localize the hole, 96% of which remains band-like. The hole contribution is thus established in symmetry and cooperativity, whereas its amplitude and the self-trapping predicted by real-time TDDFT[28] remain open.

Two residuals delimit the present description. At 0.4–0.8 ps the measured anisotropy exceeds that supplied by the structures and carriers, and at 5.14 ps the model exceeds α by 0.03 (0.571 versus 0.541 ± 0.007), where the youngest ordered R* carries half the signal. Both occur where the model is least constrained—before pM matures and where nascent R* dominates—and identify where the description of emerging order remains incomplete.

Intergrain heat flow governs phase conversion and texture

After the structural conversion is complete, the optical anisotropy continues to evolve for hundreds of picoseconds because heat flows between grains (Fig. 3d,e). At 8.6 mJ cm^{-2}, α rises from 0.59 at 15 ps to 0.70

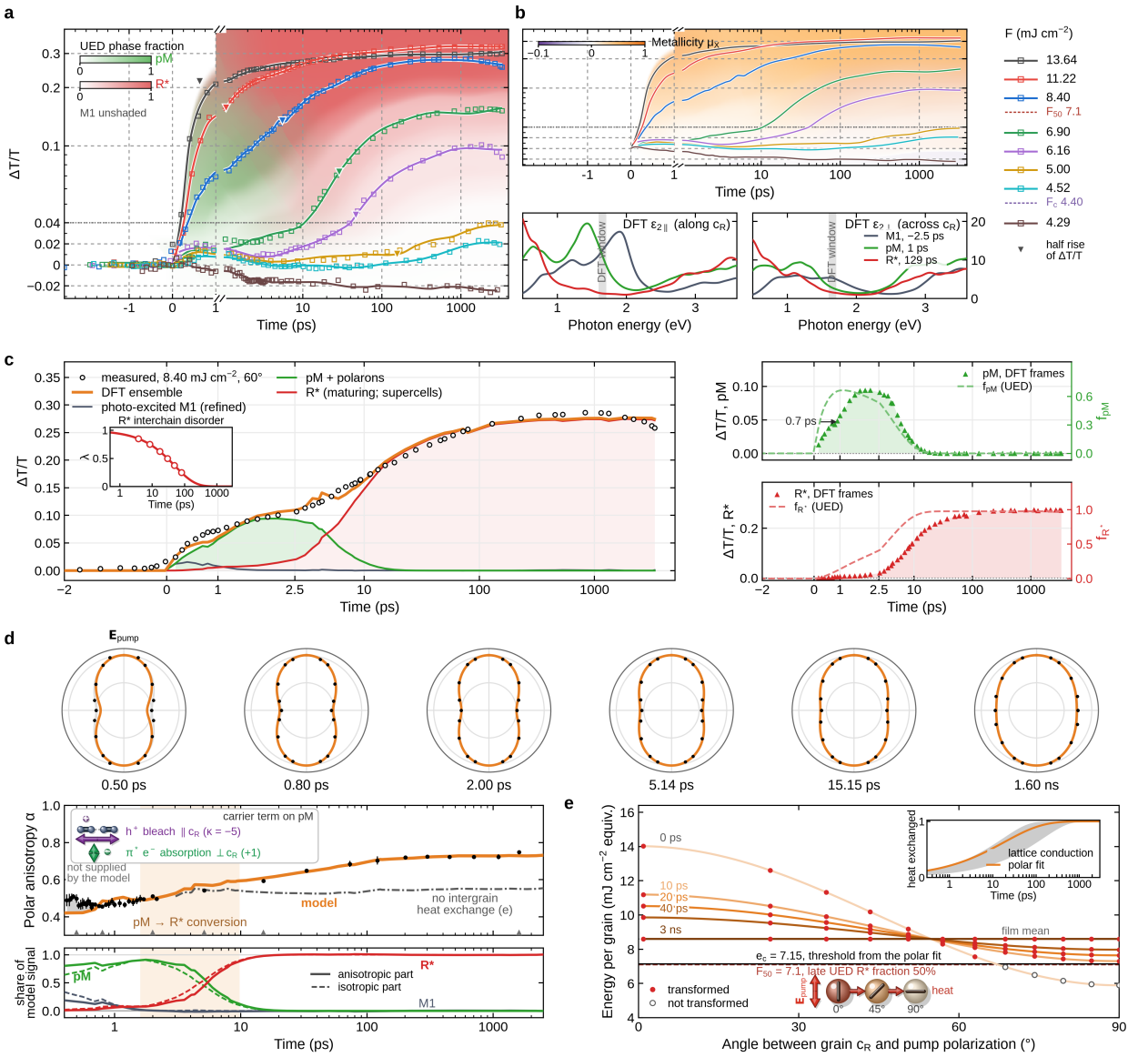


Fig. 3 | Optical measurements reveal electronic and local-order dynamics beyond the average crystal structure. **a**, ΔT/T at eight fluences (mJ cm⁻²). Squares, measured; lines, per-fluence decomposition on the UED fractions $f_X(t)$ (Methods); triangles, half rise of the measured ΔT/T. Shading, f_{pM} (green) and f_{R^*} (red); dashed, F_{c} and F_{50}. **b**, Top, the same lines with the converted volume colored by its optical metallicity relative to cold M1 (orange, more metallic; purple, less; D ×10). Bottom, DFT+U ε_2 of the refined M1 (−2.5 ps), pM (1.0 ps) and R* (129 ps) at 8.40 mJ cm⁻²; gray band, DFT readout window. **c**, ΔT/T at 8.40 mJ cm⁻² and 60° from the DFT+U tensors of the refined structures (circles, measured; orange, model; gray, green and red, photoexcited M1, pM with the carrier term, and R*). Inset, interchain disorder λ of nascent R* (circles, supercells of Extended Data Fig. 6). Right, pM and R* contributions (triangles) with their UED fractions (dashed). **d**, Polar anisotropy at 8.6 mJ cm⁻² (separate film). Top, lobes $\cos^2\theta + \alpha\sin^2\theta$ at six delays (dots, measured; gray, α ± 1 s.d.; orange, model). Middle, α(t); shaded, pM → R* conversion (1.6–9.8 ps); gray, anisotropy not supplied by the model; dash-dot, model without intergrain exchange; inset, the carrier term in the crystal frame. Bottom, shares of M1, pM and R* in the isotropic (dashed) and anisotropic (solid) model signal. **e**, Energy per grain against the angle between c_{R} and the pump polarization at 0, 10, 20 and 40 ps and 3 ns (filled, transformed; open, not); solid, e_{c} from the polar fit; dashed, F_{50}. Lower inset, grains at 0°, 45° and 90° shaded by absorbed energy, with heat flow; upper inset, fitted exchange law (orange) against lattice conduction between 40–90-nm grains (gray). Time axes linear to 1 ps (c, 2.5 ps), logarithmic beyond.

at 121 ps and 0.75 at 1.6 ns, long after the R* fraction has saturated, whereas the same model with the grain-orientation order held fixed keeps α at 0.53–0.55: the rise reflects a change in which grains respond, not in the crystallite response. With the cold-M1 absorption anisotropy of the model ($a_{\parallel}/a_{\perp}$ = 2.38), grains with c_{R} along the pump polarization absorb 1.63 times the film average and those across it 0.68 times, and heat flows from the former to the latter. Strongly excited grains cool yet remain transformed, as the film stays above the reverse transition (thermal hysteresis), whereas weakly excited grains warm and transform on reaching threshold, lowering the orientational order of the transformed volume from 0.52 to 0.27 by 3 ns.

A stretched-exponential exchange law fitted to the polar data agrees with both the diffraction threshold and ordinary lattice conduction. Its four parameters—e_{c} = 7.15 ± 0.08 mJ cm^{-2}, a response exponent of 0.99 ± 0.03, τ = 18.6 ± 2.8 ps and β = 0.49 ± 0.02—describe an exchange that begins with the conversion and is half complete at 8.8 ps, 90% at 100 ps and 98% at 300 ps. Its threshold coincides with F_{50}, and over 97% of 0.3 ps–3 ns the law lies within the parameter-free band for heat conduction between 40–90-nm grains with the literature thermal diffusivity of VO_2, 1.2–2.0 × 10^{-6} m^2 s^{-1}[29,30] (Fig. 3e, inset; Extended Data Fig. 8). No channel faster than lattice conduction is required, consistent with the anomalously low electronic thermal conductivity of metallic VO_2[30].

Heat exchanged between neighboring grains, rather than anisotropic absorption, sets the narrow width of the conversion window (Extended Data Fig. 5a). On their own absorbed energy, grains would cross e_{c} between 4.4 and 10.4 mJ cm^{-2}, whereas the late R* fraction rises from 0.02 to 0.97 within a factor of 1.7 in fluence. Allowing each grain to relax towards the mean energy of its neighborhood under the fitted exchange law, to convert while above e_{c} and to retain R* thereafter, reproduces the late fractions with one additional parameter, a conversion time of 81 ps. Below e_{c}, hot grains are drained by colder neighbors before most convert (0.003, 0.14 and 0.43 against 0.02, 0.17 and 0.40 measured at 5.00, 6.16 and 6.90 mJ cm^{-2}); above it, cold grains are lifted over threshold by hotter ones (0.94 against 0.97 at 8.40 mJ cm^{-2}).

The product of this two-threshold pathway is not uniformly metallic: a nanoscale M1-like remnant survives where long-range superlattice diffraction appears to show almost complete conversion (Extended Data Fig. 9). At 8.40 mJ cm^{-2}, the R-sensitive lattice reflections, the optical plateau relative to 11.22 mJ cm^{-2} and the late anisotropy concur on ~13% M1-like order, whereas the superlattice reflections register only 3% (0.026 ± 0.007); pockets $\lesssim$ 25 Å across reconcile the two by diverting superlattice intensity into diffuse scattering while preserving the local atomic arrangement. The converted fraction is therefore 0.85–0.90 rather than 0.97, the remnant is concentrated in the least-excited orientation class, and it is absent at 11.22 mJ cm^{-2} and above. Energy conservation further requires the latent heat of the 40–90-nm grains to be 0.5–0.7 of the bulk

value[31]; otherwise the film at 8.40 mJ cm^{-2} would fall below the cooling branch of its transition, where R* is unstable (Methods).

Discussion

VO_2 does not switch by a direct collapse between its two equilibrium phases. It switches through a transient electronically active monoclinic doorway, followed by a structurally and thermally mediated maturation of the metallic state. Figure 4a summarizes the central physical result of our multimodal reconstruction. Above the photocarrier threshold, the material begins to acquire metallic optical character while retaining most of its V–V pairing. At 8.40 mJ cm^{-2} the intermediate reaches a reconstructed fraction of 0.66 at about 1.2 ps and retains 63% of the M1 dimerization; R* subsequently overtakes it, while the optical response continues to change after the rutile-like Bragg fraction has largely saturated. A second threshold determines whether the transformed volume grows to completion. The resulting transition therefore has not one critical event but two different gates: one that permits a carrier-driven electronic pathway, and another that governs the collective structural outcome.

This sequence changes the interpretation of one of the best-studied correlated phase transitions. The prompt gap collapse established by ultrafast spectroscopy[1] describes the initiation of electronic destabilization; the monoclinic metal-like signal and stepwise structures resolved by diffraction[2,12,13] are naturally associated with the transient doorway and its conversion. Ultrafast V–V disordering[3,16] need not contradict the development of a rutile-like Bragg pattern: our supercell analysis shows how local chain distortions can survive without coherent interchain order, changing the dielectric response while leaving the average Bragg structure nearly unchanged. Heat, emphasized in earlier accounts[4], becomes essential not as the initiating cause of every electronic change, but as the mechanism capable of redistributing excitation and selecting the final conversion fraction. The advance is not to assign victory to an electronic or structural picture; it is to resolve the sequence in which electronic correlations, lattice deformation, short-range order and heat each become decisive.

The doorway also provides a microscopic basis for why the optical response cannot be inferred from the average lattice alone. DFT+U applied to the recovered atomic coordinates accounts for pronounced changes in spectral anisotropy, but no reconstructed average structure reproduces the early polarization dependence. An additional carrier contribution—hole-related bleaching along the V chains and electron-related absorption across them—resolves the principal anisotropy deficit, and charged-supercell calculations support its sign and

cooperative character. These calculations do not establish a unique, self-trapped polaron configuration or reproduce the full fitted amplitude; *polaronic* therefore denotes the experimentally motivated carrier–lattice character of the doorway, not a separately proven localization pattern. Likewise, the nascent R* supercell description identifies an optical signature compatible with locally distorted chains lacking interchain registry; the inferred one-dimensional growth morphology remains an interpretation rather than a directly imaged topology. These distinctions sharpen, rather than weaken, the principal conclusion: an atomic structure can be resolved while the electronic and local-order degrees of freedom that determine its functionality are still evolving.

The separation of initiation from completion gives optical excitation more than one physical control (Fig. 4b,c). The onset threshold near $F_c = 4.40$ mJ cm^{-2} coincides with a photo-hole density on the order of 10^{21} cm^{-3} and an optical rise that slows by a factor of 249 as this boundary is approached. In contrast, the late superlattice response and independently fitted polarization anisotropy locate the completion boundary near 7.1–7.15 mJ cm^{-2}. Because optical absorption is crystallographically anisotropic, the grains that initially cross this boundary form an oriented subset; subsequent energy exchange between neighboring grains changes the membership of that subset and thus its optical anisotropy. Pump fluence consequently selects not merely whether switching occurs, but the tempo of doorway traversal, the extent of conversion and the texture of the emergent metal. This is a structure–function principle of immediate relevance to controlling correlated phase transformations, rather than a retrospective description of their endpoints.

The scope of the evidence follows from the unusually direct confrontation between structure and function. Simultaneous diffraction and transmission define a shared experimental time axis; physics-guided inversion yields a population-resolved atomic trajectory; and first-principles dielectric tensors calculated on those coordinates expose precisely where average structures are insufficient. The carrier amplitude, the disorder-maturation timescale and aspects of the thermal mixing model are constrained using optical data and are not independent first-principles predictions. They nonetheless produce discriminating tests across structural, polarization and time-resolved measurements, while the observed separation of critical thresholds does not depend solely on an imposed kinetic gate. The work establishes a coherent account of the transition at the level supported by these constraints, without treating microscopic interpretations as measurements.

Our findings reveal a distinct organizing principle for photoinduced phase transitions: electronic instability, structural conversion and the emergence of functional order need not coincide, even when the equilibrium transformation is sharply first-order. In VO_2, photocarriers access a transient monoclinic state that retains substantial atomic pairing, subsequent lattice reorganization produces a rutile-like structure whose optical

response continues to evolve, and collective energy redistribution determines the transformed volume and texture. By reconstructing this sequence at the level of atomic structure and electronic function, we show how a hidden nonequilibrium pathway mediates the transition between equilibrium phases and establishes distinct physical conditions for its initiation and completion. The resulting perspective shifts the control of correlated phase transitions from selecting their equilibrium endpoints toward understanding—and ultimately manipulating—the transient states through which metallic functionality emerges.

Methods

Samples and dual-probe measurements

Polycrystalline VO_2 films, consisting of grains 40–90 nm across supported on 9-nm SiN_x membrane windows, were grown and characterized as in ref.[18]. Scanning transmission electron microscopy shows randomly oriented grains, each single-crystalline up to its boundary (Fig. 1a). Measurements were made in the UEM-1 instrument[21]: a 1.55-eV pump pulse (35 fs full width at half maximum, FWHM; 100-μm FWHM spot; 200-Hz repetition rate) excites the film, and a 60-keV electron pulse of about 10^4 electrons from a high-brightness pancake-beam source[19,20] and an 800-nm optical pulse in transmission probe it under the same excitation on one time axis. The instrument responses are < 50 fs (UED)[21] and 35 fs (OPP), FWHM. Powder patterns were radially averaged over $s \approx 1.8$–5.5 Å^{-1}, where 21 reflections are resolved, 17 of which serve as intensity channels and seven as peak-position channels. Eight fluences (4.29, 4.52, 5.00, 6.16, 6.90, 8.40, 11.22 and 13.64 mJ cm^{-2}) were recorded to 3.3 ns, together with a densely sampled short-window dataset at 8.0 mJ cm^{-2} extending to approximately 4 ps. The polarization dependence of the transmission was measured in separate experiments under the same physical conditions, at θ_{PP} = 15, 25, 47, 71 and 90° and six fluences between 8.0 and 9.7 mJ cm^{-2} on a common fluence scale; it supplies additional constraints on the anisotropy of the response and on its depolarization by intergrain energy transport.

Physics-guided inversion of diffraction

Structural model. Each phase is described in the 12-atom cell of M1 (space group $P2_1/c$). The vanadium positions follow from two order parameters, the dimerization d_r and the twist d_w; the oxygen positions carry a displacement δO(t) shared by all phases; and the lattice of each frame follows from the seven peak-position channels through four strain channels, with the cold M1 lattice calibrated to the bulk structure[32]; the late R*

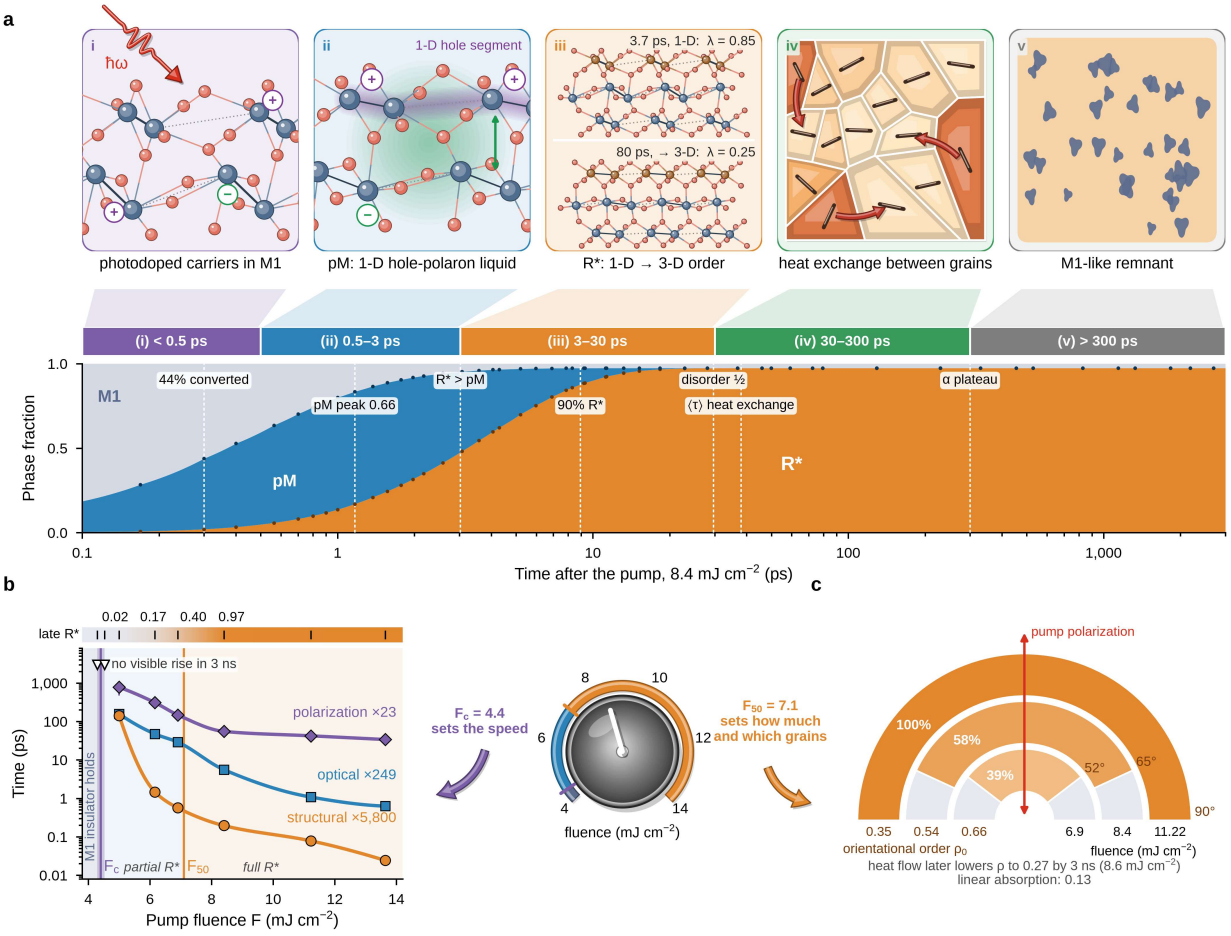


Fig. 4 | Distinct electronic and thermal thresholds govern the pathway and outcome of ultrafast switching. **a**, The transition at 8.4 mJ cm^{-2} in five stages (i, iv and v schematic): (i) the pump pulse dopes holes (+) onto the V–V dimers and electrons (−) into π* states of cold M1; (ii) pM on its refined lattice, with holes condensed along one chain (purple) and π* electrons delocalized across the chains (green); (iii) computed R* supercells (V blue and brown, the two signs of the local distortion) at 3.7 ps (λ = 0.85), with M1-like pairing uncorrelated between chains, and at 80 ps (λ = 0.25), where it has faded; (iv) grains whose c_R axis (bar) lies along the pump polarization absorb more and pass heat to their neighbors (color, absorbed energy); (v) 13% of the film keeps M1-like order in pockets $\lesssim$ 25 Å across. Bottom, UED phase fractions (dots; gray, M1; blue, pM; orange, R*) under the time span of each stage. **b**, The fluence sets the speed: time for the R* fraction to reach 1% (circles; kinetic model), for ΔT/T to reach half its plateau (squares) and depolarization time (diamonds); lines, guides labeled with the speed-up from 5.0 to 13.6 mJ cm^{-2}. Triangles, no rise within 3 ns (4.29 and 4.52 mJ cm^{-2}); purple band, F_c. Top strip, late R* fraction (1–3 ns), crossing one half at F_{50}. Center, fluence dial with both thresholds (pointer, 8.4 mJ cm^{-2}). **c**, The fluence sets the orientation: grains by the angle between c_R and the pump polarization (vertical); orange, grains whose absorbed energy exceeds e_c at 6.9, 8.4 and 11.2 mJ cm^{-2} (inner to outer ring); left numbers, orientational order ρ_0 of the transformed volume (0.13 for linear absorption). λ, exchange times, cones and ρ_0 are modeled (Fig. 3); all other quantities are measured or refined.

cell is refined from the shifts of the same seven peaks, indexed on the rutile reflections that fall in each, with a single tetragonal cell (Extended Data Fig. 3; Supplementary Note 1). The vanadium motifs of M1 and pM were refined freely in earlier iterations of the workflow (per-fluence d_r^{pM} = 0.867–0.972 and d_w^{pM} = 0.50–0.63) and are held at their converged values in the final inversion (M1, d_r = 1.0595, d_w = 1.131; pM, d_r = 0.902, d_w = 0.514), which reduces degeneracy between structure and kinetics; the R* vanadium coordinates, the oxygen displacement, the lattice and the Debye–Waller factors are refined at every frame.

Kinetics. The volume fractions of M1, pM, R* and a structureless defect phase D obey

$$\frac{df_i}{dt} = \sum_{\text{edges}} (J_{\text{in}} - J_{\text{out}}), \qquad J_{\text{M1}\to\text{pM}} = k_1 f_{\text{M1}} e^{-t/\tau_p}, \qquad J_{\text{pM}\to\text{R*}} = g_{\text{fil}}(t;F)\, f_{\text{pM}} \left[k_b + k_n\, \sigma\!\left(\frac{f_{\text{pM}} - f_c}{\delta}\right) \left(\frac{f_{\text{pM}}}{f_c}\right)^{m-1} \right. \tag{1}$$

with $f(0)$ = (1, 0, 0, 0). The rates scale with fluence relative to F_{ref} = 8.0 mJ cm^{-2}, and the pM → R* channel passes a critical gate that is closed for $F \le F_c$ and opens as $[(F - F_c)/(F_{\text{ref}} - F_c)]^{\beta}$ above it (F_c inferred within the optical bracket 4.29–4.52 mJ cm^{-2}, 4.40 at convergence; β = 2.34). The final fractions are multiplied by an excitation-volume factor η(F), a skew-normal cumulative distribution anchored to the measured superlattice order parameter, with no free parameter, and the filament gate g_{fil} delays the pM → R* flux above F_c on a time proportional to the optical depolarization time. Because the critical gate and η(F) are imposed, the fluence dependence of the refined fractions, and in particular their slowing near F_c, is used only where the measured observables (the optical half-rise time and the superlattice intensities) agree with it. The Avrami exponent of the R* rise is 0.95–1.2, depending on the fit window.

Diffraction. Intensities are computed with Doyle–Turner electron form factors, evaluated at $s^2 = (\sin\theta/\lambda)^2$ (the correction that distinguishes the adopted refinement from an earlier one), and with Blackman two-beam dynamical scattering averaged over grain thicknesses of 50–90 nm in 21 bins[33,34]. Two overlapping reflections (s = 3.645 and 3.791 Å^{-1}) are blended with a measured overlap constant of 0.4272. Debye–Waller factors are refined as differentials relative to the pre-time-zero structure.

Neural-network inversion. A surrogate encoder—two one-dimensional convolution layers (17 → 128 → 64 channels), a bidirectional LSTM (hidden size 64) and output heads for kinetics, structure, lattice and Debye–Waller parameters—maps the 17 intensity traces of each data set onto a 36-dimensional latent vector shared by all data sets except for the fluence. It is trained on 20,000 simulations of the forward model with a composite loss on reconstructed intensities, simplex closure and non-negativity of the fractions, causal ordering (R* after

pM; irreversible defect accumulation) and temporal smoothness, in a five-stage curriculum that frees kinetic, threshold, structural and finally all parameters from warm-started backbones; the checkpoint with the lowest validation loss is used. Optical constraints are built into the forward model that generates the training data: the critical fluence is bracketed by the sign reversal of the optical order parameter, the pM → R* conversion is gated on the optical depolarization time, and a differentiable phase-resolved optical forward model couples the inferred fractions to ΔT/T, so that the structural inversion is optically consistent by construction. In the final generation the measured optical traces were withheld from the training loss, so that their reproduction from the refined structures through DFT+U (below) constitutes an independent test of the inversion.

Post-inference refinement. Starting from the inferred intensities, a chain of least-squares refinements is applied to each fluence: Debye–Waller factors (a harmonic relaxing-deviator model; 6 global, 1 time-constant, 45 deviator and $3T$ isotropic parameters for T frames after time zero), the R* vanadium order parameters ($2T$), the shared oxygen displacement ($6T$), a second Debye–Waller pass and Gaussian smoothing of the coordinates in time (σ = 0.5 ps; 0.1 ps for the short-window sets). Against 17 intensity and 7 position channels per frame, the refinement is overdetermined by more than a factor of two. The refined Debye–Waller deviators fail full-tensor positivity in many frames and partly absorb mean-structure misfit; they are treated as an intensity correction, and no conclusion of this work rests on them. The weighted-profile R factor of the adopted refinement is $R_{\mathrm{wp}} = 0.031$.

Regularized oxygen trajectory at 8.40 mJ cm⁻². The shared oxygen displacement makes a 0.06–0.07-Å excursion at 0.30–1.00 ps, which kinks the computed ΔT/T near 1 ps. For the optical model it was refitted over 0–2.2 ps with a penalty on its change between frames, within the χ^2 budget of the refinement's smoothing step; about half of the excursion remains (removing it raises χ^2 by 609 over 238 points). Fig. 2c and Extended Data Fig. 4 show the refined structures.

Coherent phonons

The six oxygen-displacement channels of the 8.0 mJ cm⁻² refinement (0.05–2.5 ps, 276 points) and the five optical traces (0.05–0.70 ps, 165 points) are fitted with three damped oscillators. The diffraction channels share one frequency f_0 and one damping rate per mode; the optical traces share the same modes, with frequency $f_0 - \beta \cos 2\theta_{\mathrm{PP}}$ and one damping rate per mode; amplitudes, phases and one slow term are free per trace. Each model trace is convolved with a Gaussian response, 50 fs FWHM for the diffraction channels and an effective 200 fs for the optical traces; each trace is weighted by its own noise, and a fifth-order polynomial

background is removed over each window (13 shared and 77 per-trace parameters; reduced χ^2 0.93). The UED time zero was calibrated from the onset of the intensity change (±50 fs); profile likelihoods give β_2 = +0.06 (−0.08 to +0.21) and β_3 = +0.10 THz (0.00 to +0.19), and $\beta_3 \leq -0.3$ THz is excluded ($\Delta\chi^2 \geq 8.5$). At the earliest UED delays (0.05–0.08 ps apart) the 7.46-THz term approaches the sampling limit. Density-functional perturbation theory of the photoexcited structure and the mode assignment are given in Extended Data Fig. 2 and Supplementary Note 1; modes are assigned by displacement character, not by the nearest DFPT frequency.

DFT+U calculations

Dielectric tensors were computed with Quantum ESPRESSO 7.2[35,36] (pw.x and epsilon.x) on the refined 12-atom cells, without relaxation or symmetrization, using the PBE functional with norm-conserving pseudopotentials (V with 3s3p semicore), 80/320 Ry cut-offs, a Hubbard U = 3.5 eV on V 3d (ortho-atomic projectors), a 6 × 6 × 6 k-point mesh for both the self-consistent and the non-self-consistent step, 120 bands, Fermi–Dirac occupations at 300 K (0.0019 Ry) and the independent-particle approximation (epsilon.x, 0–10 eV in 1,000 steps, 0.05-eV interband broadening). Spectra are re-broadened to 0.20 eV and weighted by a Gaussian at 725–775-nm window (1.60–1.71 eV), shifted from the 800-nm (1.55-eV) probe to compensate for the known offset of the interband edges DFT+U underestimates, and this window is the one in which the computed responses of cold M1 and R pass the consistency check against the calibrated film optical readout. A common scale cancels from α and is absorbed by K. DFT overestimates ε_2 of cold M1 at the probe by a factor of 2–3 relative to film optics, mostly through a strong $d_{\parallel}$ interband peak at 1.6–1.8 eV; the probe-side outputs are insensitive to this, and the pump-side dose uses the measured film optics. The R* supercells are 1 × 4 × 2 tilings (96 atoms, 16 chains; k-mesh 6 × 2 × 3, 960 bands) of the refined R* of the delay at which λ(t) passes each node (λ = 0.85, 0.75, 0.625, 0.5, 0.375 and 0.25); each chain j carries $\mathbf{R}^*(t_\lambda) + (s_j - m)\, a\, \lambda\, \delta^{\mathrm{M1}}$ with $s_j = \pm 1$, where δ^{M1} is the antiphase vanadium distortion of cold M1, m = ¼ the net pairing of the refined R* and a = 0.851 the largest amplitude allowed by the measured vanadium Debye–Waller excess; oxygen atoms and the lattice remain at R* (Extended Data Fig. 6; Supplementary Note 1). The charged-hole cells are 32-V (96-atom) cells with frozen geometries (spin-unpolarized, U = 3.5 eV), with one to four holes placed on isolated, chain-condensed, neighboring-chain or dispersed unpaired dimers; the carrier response is the difference between each charged cell and its neutral twin, and the pristine cell reproduces the 12-atom cold-M1 tensor to better than 0.01%.

Optical forward model

Each phase volume carries the DFT+U tensor of its refined cell at that delay; the film tensor follows from an effective-medium mixture weighted by f_X (Maxwell-Garnett–Bruggeman crossover, spherical inclusions), applied separately to the components along and across c_{R}, and ΔT/T is evaluated against the cold-M1 film at the probe geometry. One scale factor K per film is profiled by linear least squares. The photoexcited M1 carries the refined M1 cell of each frame. The pM and R* channels are

$$\varepsilon_{\mathrm{pM}}(t) = \tilde{\varepsilon}_{\mathrm{pM}}(t) + c_{\mathrm{age}}(t)\left[\varepsilon^{\mathrm{struct}}_{\mathrm{R}^*}(t) - \tilde{\varepsilon}_{\mathrm{pM}}(t)\right] + \Delta\varepsilon_{\mathrm{pol}}, \qquad \tilde{\varepsilon}_{\mathrm{pM}} = \varepsilon^0_{\mathrm{M1}} + g(t)\left[\varepsilon^{\mathrm{cell}}_{\mathrm{pM}}(t) - \varepsilon^0_{\mathrm{M1}}\right], \quad (2)$$

$$\varepsilon_{\mathrm{R}^*}(t) = \left[1 - w_{\mathrm{imm}}(t)\right]\left[\varepsilon^{\mathrm{struct}}_{\mathrm{R}^*}(t) + w_{\mathrm{R}}(t)\,\Delta\varepsilon_{\mathrm{pol}}\right] + w_{\mathrm{imm}}(t)\,\varepsilon_{\mathrm{M1}}(t), \qquad \varepsilon^{\mathrm{struct}}_{\mathrm{R}^*}(t) = \varepsilon^{\mathrm{cell}}_{\mathrm{R}^*}(t) + \Delta(\lambda(t)), \quad (3)$$

with $g = 1 - e^{-t/\tau_{\mathrm{mat}}}$ (τ_{mat} = 1 ps; new pM starts from the cold-M1 response), $c_{\mathrm{age}} = 1 - e^{-t/\tau_{\mathrm{age}}}$ (τ_{age} = 10 ps), $\lambda(t) = \lambda_0 \exp[-(t/\tau_{\mathrm{c}})^b]$ (λ_0 = 1, τ_{c} = 50 ps, b = 0.7) and Δ(λ) the dielectric excess of the supercells over the refined R*, interpolated (PCHIP) between nodes. The age kernels $w_\tau(t) = \int_0^t f'_{\mathrm{R}^*}(s)\, e^{-(t-s)/\tau}\, ds \,/\, f_{\mathrm{R}^*}(t)$ give the share of the R* volume converted within the last ~τ: w_{imm} with τ = 2 ps (newly converted R*, without interchain order, responds like the photoexcited M1) and w_{R} with τ_{R} = 10 ps. The carrier term is

$$\Delta\varepsilon_\perp(E) = A\,\frac{L(E)}{\mathrm{Im}\,L(E_{\mathrm{p}})}, \qquad \Delta\varepsilon_\parallel = \kappa\,\Delta\varepsilon_\perp, \qquad L(E) = \frac{1}{E_{\mathrm{c}}^2 - E^2 - i\Gamma E}, \quad (4)$$

so that A is the change of $\varepsilon_{2\perp}$ at the probe energy E_{p} = 1.653 eV; A = 1 (π* electron absorption across the chains) and κ = −5 (hole bleach of the dimer transition along them), with E_{c} = 1.82 eV and Γ = 0.5 eV fixing only the Kramers–Kronig partner. No carrier term is applied to the photoexcited M1 or to immature R*; free carriers otherwise enter only through the DFT tensors. The 60° traces at 8.40 mJ cm^{-2} (67 delays to 3.3 ns) and 8.0 mJ cm^{-2} (58 delays to 2.5 ps) are fitted jointly. The decomposition of Fig. 3a,b is a separate, per-fluence linear least-squares fit of ΔT/T on the UED fractions, a hot-electron term and the refined lattice; its coefficients define the optical metallicity μ_X of each phase relative to cold M1 and are not unique where columns are collinear. It reaches R^2 = 0.922–0.999 over the eight fluences (0.999, 0.999, 0.999 and 0.929 at 11.22, 8.40, 6.90 and 4.29 mJ cm^{-2}).

Optical polar readout and intergrain exchange

The polar arrays are reduced per delay to $\Delta T/T(\theta,t) = S(t)[\cos^2\theta + \alpha(t)\sin^2\theta] + C_0$, giving 219 values of α between 0.5 and 800 ps. For randomly oriented grains

$$\alpha = \frac{1-\frac{2}{3}x}{1+\frac{4}{3}x}, \qquad x = \rho_{\text{eff}}\, D, \qquad D = \frac{3}{2}\,\frac{1-r}{1+2r}, \quad r = \frac{\Delta\varepsilon_{2\perp}}{\Delta\varepsilon_{2\parallel}}, \tag{5}$$

where $D(t)$ is the crystallite anisotropy of the model of Eq. (2) and Eq. (3) and ρ_{eff} the orientational order of the responding grains. A grain whose c_{R} axis makes an angle θ_{c} with the pump polarization ($c = \cos\theta_{\text{c}}$) absorbs

$$e_0(c) = F\,\frac{a(c)}{\bar{a}}, \qquad a(c) = a_\parallel c^2 + a_\perp(1-c^2), \qquad \bar{a} = \tfrac{1}{3}(a_\parallel + 2a_\perp), \tag{6}$$

with $a_\parallel/a_\perp$ = 2.38, the ratio of ε_2 of the cold M1 of the model along and across c_{R} (19.24/8.08). Energy is exchanged in the mean field and each grain responds with memory of its peak energy:

$$e(c,t) = F + [e_0(c) - F]\,\varphi(t), \qquad \varphi(t) = e^{-(t/\tau)^\beta}, \qquad g = [\max(e_0, e) - e_{\text{c}}]_+^{\,p}, \qquad \rho_{\text{eff}} = \frac{\langle g\,P_2(c)\rangle}{\langle g\rangle}. \tag{7}$$

A stretched exponential with $0 < \beta \le 1$ is a positive mixture of exponential relaxations, as expected when the exchange time varies from grain to grain; the mean time is $\tau\,\Gamma(1+1/\beta)$. The four parameters are fitted jointly to the 219 values of α with the optical model fixed: e_{c} = 7.15 ± 0.08 mJ cm^{-2}, p = 0.99 ± 0.03, τ = 18.6 ± 2.8 ps and β = 0.49 ± 0.02 (mean exchange time 38 ps; half exchange at 8.8 ps). Without memory, α tends to 1 at late times, which the data reject. The fitted kernel is compared with conduction in a checkerboard of cubic grains of edge ℓ in perfect contact,

$$\varphi_\ell(t) = \left[\frac{8}{\pi^2}\sum_{n\ge 0}\frac{\exp(-(2n+1)^2\pi^2 D_{\text{th}}t/\ell^2)}{(2n+1)^2}\right]^3, \tag{8}$$

the product of three slab solutions of the heat equation[37], with ℓ = 40–90 nm (electron microscopy of these films) and $D_{\text{th}} = \kappa_{\text{th}}/C$ = 1.2–2.0 × 10^{-6} m^2 s^{-1} from κ_{th} = 3.5–6 W m^{-1} K^{-1}[29,30] and C = 3.0 J cm^{-3} K^{-1}[29,31].

Interface (Kapitza) resistance can only slow conduction[38]. The fitted exchange lies inside this band over 97% of 0.3 ps–3 ns.

Thresholds, times and cones

F_c = 4.40 mJ cm^{-2} (bracket 4.29–4.52) is the fluence at which the long-time order parameter of the OPP changes sign. The absorbed dose is $u = (A/d)F$, with absorbed fraction A = 0.28–0.39 and A/d = 3.2–7.0 × 10^4 cm^{-1} for 40–90-nm films on SiN_x, from a transfer-matrix calculation with the measured film optics at 800 nm (refractive index 2.85, penetration depth 100 nm)[18]; d = 40–90 nm is the grain size of these films. One hole–electron pair per absorbed 1.55-eV photon gives a photo-hole density of 0.6–1.3 × 10^{21} cm^{-3} (0.017–0.037 per V) at F_c and 1.1–2.4 × 10^{21} cm^{-3} at 8.40 mJ cm^{-2}. The Mott criterion $n_c^{1/3} a_B^* \approx 0.26$ gives $n_c \approx 10^{21}$ cm^{-3} for electronic screening ($\varepsilon \approx 8$) and an effective mass of 1.5–2 m_e, both from our DFT+U calculations. The optical half-rise time is the delay at which the measured 60° $\Delta T/T$ last rises through half its plateau (mean beyond 100 ps); it is not defined where $\Delta T/T$ stays below 0.03 within 3 ns (4.52 mJ cm^{-2}) or the late signal is negative (4.29 mJ cm^{-2}); the R* onset time is the delay at which the refined R* fraction first exceeds 1% (a property of the kinetic model, above); the depolarization time is that of the optical decomposition refitted at each fluence (well identified for $F \geq 5.0$ mJ cm^{-2}). The cones of Fig. 4c are the grains whose prompt absorbed energy $e_0(c)$ exceeds e_c before any exchange, with $\rho_0 = \langle g P_2(c) \rangle / \langle g \rangle$.

The late R* fraction (mean over 1–3 ns) crosses one half at F_{50} = 7.07 mJ cm^{-2} (error-function fit over the eight fluences) to 7.17 mJ cm^{-2} (linear interpolation between 6.90 and 8.40). For Extended Data Fig. 5a each grain relaxes toward the mean energy m of its neighborhood, $e(t) = m + (e_0 - m)\exp[-(t/\tau)^\beta]$, with τ and β of the polar fit and m the mean over the grain and its six in-plane neighbors (the lattice diffusion length at 1–3 ns is about one grain); it converts at rate k_0 while its energy exceeds e_c and retains R* thereafter (hysteresis). The one fitted parameter is $1/k_0$ = 81 ps (sum of squared residuals 0.0033, against 0.18 for conversion on each grain's own energy at the same e_c).

Remnant and energy budget

At 8.40 mJ cm^{-2} it is estimated from (i) the $(30\bar{2})$ superlattice reflection, 0.026 ± 0.007; (ii) the R-sensitive lattice reflections against 11.22 and 13.64 mJ cm^{-2}, 0.10–0.15; (iii) the late optical plateau per converted volume, 13.6% below that at 11.22 mJ cm^{-2}; and (iv) the late anisotropy at 8.6–8.8 mJ cm^{-2}, which requires 0.111–0.125 at M1 contrast in one orientation class. In a kinematic simulation of a film of 32^3 M1 cells,

single-variant pockets of 13% volume grown last from random R* nuclei (mean chord 13 Å) read 0.01–0.02 on $(30\bar{2})$ and 0.13–0.14 on the R-sensitive lattice reflections (Extended Data Fig. 9a). The energy budget uses $u = (A/d)F$; full conversion requires 372 J cm^{-3}, of which the bulk latent heat is 235 J cm^{-3}[31] and the sensible heat to the transition (338 K) 136 J cm^{-3}[18]. The late film temperature $T = 298\,\mathrm{K} + (u - fL)/C$ remains at or above the cooling branch (≈ 330 K) at 8.40 mJ cm^{-2} only if $L_{\mathrm{film}} \leq 0.70\,L_{\mathrm{bulk}}$ (A/d = 3.2 × 10^4 cm^{-1}) or $\leq 0.85\,L_{\mathrm{bulk}}$ (3.6 × 10^4 cm^{-1}).

Parameters and limitations

The parameters of the optical and exchange models, how each was set and the data that constrain it are listed in Supplementary Table 1. In total, two continuous scale factors, nine time constants or amplitudes chosen from discrete grid scans and four least-squares exchange parameters are set against 344 optical data points (125 at 60°, 219 polar), with the phase fractions and structures fixed by diffraction. Fit quality: 60° RMSE/R^2 0.0089/0.988 (8.40 mJ cm^{-2}, 67 delays) and 0.0105/0.825 (8.0 mJ cm^{-2}, ≤ 2.5 ps); polar χ^2/n 2.41 (0.5–1.9 ps 2.65, 1.9–20 ps 3.07, 20–800 ps 1.12).

Data availability

The data are available from the corresponding author upon reasonable request.

Code availability

The code for the physics-guided inversion (forward operators, encoder, training curriculum and post-inference refinement) and the first-principles optical model is part of a research framework under active development and is not yet publicly released; it is available from the corresponding author upon reasonable request. The figure scripts are provided with the source data. Quantum ESPRESSO is open-source software[35,36].

References

1. Wegkamp, D. *et al.* Instantaneous band gap collapse in photoexcited monoclinic VO2 due to photo-carrier doping. *Phys. Rev. Lett.* **113**, 216401 (2014).

2. Morrison, V. R. *et al.* A photoinduced metal-like phase of monoclinic VO2 revealed by ultrafast electron diffraction. *Science* **346**, 445–448 (2014).

3. Wall, S. *et al.* Ultrafast disordering of vanadium dimers in photoexcited VO2. *Science* **362**, 572–576 (2018).

4. Vidas, L. *et al.* Does VO2 host a transient monoclinic metallic phase? *Phys. Rev. X* **10**, 031047 (2020).

5. Samizadeh Nikoo, M. *et al.* Electrical control of glass-like dynamics in vanadium dioxide for data storage and processing. *Nat. Electron.* **5**, 596–603 (2022).

6. Duan, X. *et al.* Reconfigurable multistate optical systems enabled by VO2 phase transitions. *ACS Photonics* **7**, 2958–2965 (2020).

7. Goodenough, J. B. The two components of the crystallographic transition in VO2. *J. Solid State Chem.* **3**, 490–500 (1971).

8. Zylbersztejn, A. & Mott, N. F. Metal-insulator transition in vanadium dioxide. *Phys. Rev. B* **11**, 4383–4395 (1975).

9. Eyert, V. The metal-insulator transitions of VO2: A band theoretical approach. *Ann. Phys.* **11**, 650–704 (2002).

10. Biermann, S., Poteryaev, A., Lichtenstein, A. I. & Georges, A. Dynamical singlets and correlation-assisted Peierls transition in VO2. *Phys. Rev. Lett.* **94**, 026404 (2005).

11. Haverkort, M. W. *et al.* Orbital-assisted metal-insulator transition in VO2. *Phys. Rev. Lett.* **95**, 196404 (2005).

12. Otto, M. R. *et al.* How optical excitation controls the structure and properties of vanadium dioxide. *Proc. Natl Acad. Sci. USA* **116**, 450–455 (2019).

13. Baum, P., Yang, D.-S. & Zewail, A. H. 4D visualization of transitional structures in phase transformations by electron diffraction. *Science* **318**, 788–792 (2007).

14. Cavalleri, A., Dekorsy, T., Chong, H. H. W., Kieffer, J. C. & Schoenlein, R. W. Evidence for a structurally-driven insulator-to-metal transition in VO2: A view from the ultrafast timescale. *Phys. Rev. B* **70**, 161102 (2004).

15. Wall, S. *et al.* Ultrafast changes in lattice symmetry probed by coherent phonons. *Nat. Commun.* **3**, 721 (2012).

16. de la Peña Muñoz, G. A., Correa, A. A., Yang, S. & Delaire, O. Ultrafast lattice disordering can be accelerated by electronic collisional forces. *Nat. Phys.* **19**, 1489–1494 (2023).

17. Tao, Z. S. *et al.* Decoupling of structural and electronic phase transitions in VO2. *Phys. Rev. Lett.* **109**, 166406 (2012).

18. Tao, Z. *et al.* The nature of photoinduced phase transition and metastable states in vanadium dioxide. *Sci. Rep.* **6**, 38514 (2016).

19. Portman, J. *et al.* Computational and experimental characterization of high-brightness beams for femtosecond electron imaging and spectroscopy. *Appl. Phys. Lett.* **103**, 253115 (2013).

20. Williams, J. *et al.* Active control of bright electron beams with RF optics for femtosecond microscopy. *Struct. Dyn.* **4**, 044035 (2017).

21. Sun, X. *et al.* Precision-controlled ultrafast electron microscope platforms. A case study: Multiple-order coherent phonon dynamics in 1T-TaSe2 probed at 50 fs–10 fm scales. *Struct. Dyn.* **11**, 024305 (2024).

22. Raissi, M., Perdikaris, P. & Karniadakis, G. E. Physics-informed neural networks: A deep learning framework for solving forward and inverse problems involving nonlinear partial differential equations. *J. Comput. Phys.* **378**, 686–707 (2019).

23. Karniadakis, G. E. *et al.* Physics-informed machine learning. *Nat. Rev. Phys.* **3**, 422–440 (2021).

24. Peng, L.-M., Dudarev, S. L. & Whelan, M. J. *High Energy Electron Diffraction and Microscopy*. vol. 61 (Oxford University Press on Demand, 2004).

25. Mott, N. F. *Metal-Insulator Transitions*. (Taylor & Francis, London ; New York, 1990).

26. Avrami, M. Kinetics of phase change. I general theory. *J. Chem. Phys.* **7**, 1103–1112 (1939).

27. Avrami, M. Kinetics of phase change. II transformation-time relations for random distribution of nuclei. *J. Chem. Phys.* **8**, 212–224 (1940).

28. Guo, F.-W. *et al.* Photoinduced hidden monoclinic metallic phase of VO2 driven by local nucleation. *Nat. Commun.* **16**, 94 (2025).

29. Oh, D.-W., Ko, C., Ramanathan, S. & Cahill, D. G. Thermal conductivity and dynamic heat capacity across the metal-insulator transition in thin film VO2. *Appl. Phys. Lett.* **96**, 151906 (2010).

30. Lee, S. *et al.* Anomalously low electronic thermal conductivity in metallic vanadium dioxide. *Science* **355**, 371–374 (2017).

31. Berglund, C. N. & Guggenheim, H. J. Electronic properties of VO2 near the semiconductor-metal transition. *Phys. Rev.* **185**, 1022–1033 (1969).

32. Longo, J. M. & Kierkegaard, P. A refinement of the structure of VO2. *Acta Chem. Scand.* **24**, 420–426 (1970).

33. Blackman, M. On the intensities of electron diffraction rings. *Proc. R. Soc. Lond. A* **173**, 68–82 (1939).

34. Doyle, P. A. & Turner, P. S. Relativistic Hartree–Fock X-ray and electron scattering factors. *Acta Crystallogr. A* **24**, 390–397 (1968).

35. Giannozzi, P. *et al.* QUANTUM ESPRESSO: A modular and open-source software project for quantum simulations of materials. *J. Phys.: Condens. Matter* **21**, 395502 (2009).

36. Giannozzi, P. *et al.* Advanced capabilities for materials modelling with Quantum ESPRESSO. *J. Phys.: Condens. Matter* **29**, 465901 (2017).

37. Carslaw, H. S. & Jaeger, J. C. *Conduction of Heat in Solids*. (Oxford University Press, Oxford, 1959).

38. Swartz, E. T. & Pohl, R. O. Thermal boundary resistance. *Rev. Mod. Phys.* **61**, 605–668 (1989).

Acknowledgements

The authors acknowledge useful discussions with Prof. Sheng Meng and Prof. Sokrates Pantelides on DFT calculations. The work was funded by the U.S. Department of Energy, Grant DE-FG0206ER46309. The experimental facility was supported by U.S. National Science Foundation, Grant DMR 1625181.

Author contributions

C.-Y.R. conceived and supervised the project. X.S. designed and built the dual-probe ultrafast electron diffraction and optical pump–probe platform. A.N.S. and I.G.-A grew the VO_2 films, and K.S. performed their STEM characterization. X.S., S.S. and C.-Y.R. performed the diffraction and optical measurements. C.-Y.R. and T.D.N. developed the machine-learning-guided inversion and performed the structural refinements. C.-Y.R. performed the DFT+U calculations. X.S., S.S., C.-Y.R. and T.D.N. analyzed the data. X.S. and C.-Y.R. wrote the manuscript with input from all authors.

Competing interests

The authors declare no competing interests.

Additional information

Supplementary information. The online version contains supplementary material (Supplementary Table 1 and Supplementary Note 1) available at [URL to be assigned].

Correspondence and requests for materials should be addressed to Chong-Yu Ruan (ruanc@msu.edu).

Extended Data

Supplementary Information

Table 1: Supplementary Table 1 | Parameters of the optical and exchange models, how each was set and the data that constrain it (Methods).

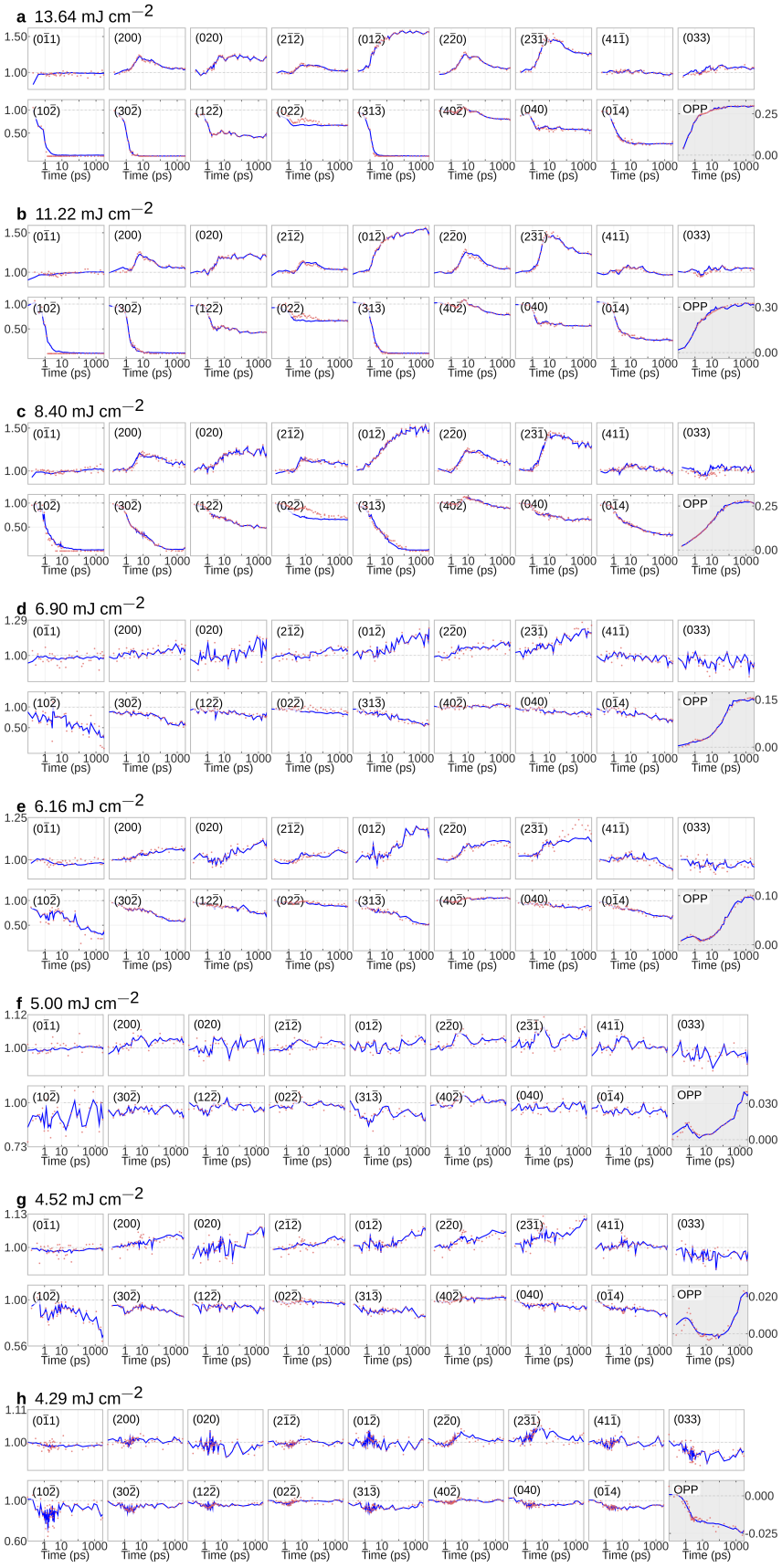
block	parameter	value	what set	constrained by
inversion	$f_X(t)$, refined cells per frame	—	refinement	diffraction (17 reflections, 8 + 2 data sets)
optics	K per film (2)	0.353, 0.304	linear least squares	60° OPP, 125 delays
optics	DFT scale, broadening, EMT	0.65, 0.20 eV	fixed	—
pM	τ_{mat} (exponent 1)	1 ps	grid-select	60° OPP + polar
pM	τ_{age}	10 ps	grid-select	60° OPP
R*	λ_0, τ_c, b	1, 50 ps, 0.7	grid-select	60° OPP
R*	maturation time	2 ps	grid-select	60° OPP
carriers	A ($\perp$), κ ($\parallel$ = κA); E_c 1.82 eV, Γ 0.5 eV fixed	1, −5	grid-select	A: 60° OPP; κ: polar
carriers	τ_R (term on R* converted from pM)	10 ps	gri-selectd	60° OPP

block	parameter	value	what set	constrained by
exchange	e_c	7.15 ± 0.08 mJ cm^{-2}	least squares	polar, 219 values
exchange	τ, β	18.6 ± 2.8 ps, 0.49 ± 0.02	least squares	polar, 219 values
exchange	p	0.99 ± 0.03	least squares	polar, 219 values
dose	$a_{\parallel}/a_{\perp}$	2.38	DFT (cold M1 of the model)	—
late fraction	$1/k_0$ (neighborhood of 7 grains, fixed)	81 ps	least squares	late R* fraction, 8 fluences

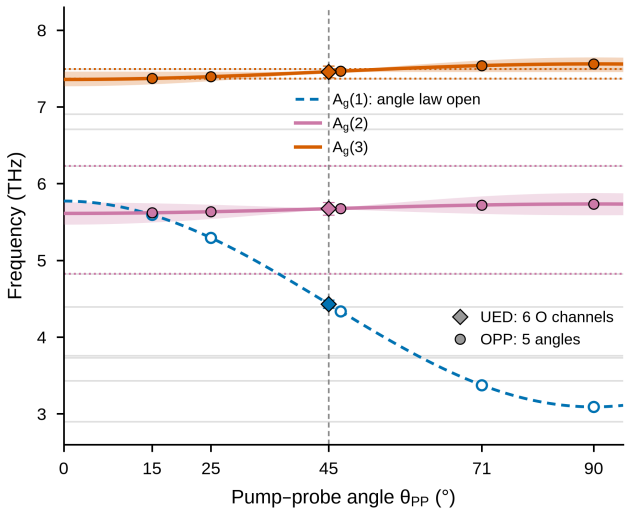
Supplementary Note 1: Computational details

Phonon calculation (Extended Data Fig. 2). Quantum ESPRESSO 7.2 (pw.x, ph.x, dynmat.x)[35,36]; PBE+U with U = 3.5 eV on V 3d (atomic-orbital projectors); norm-conserving Troullier–Martins pseudopotentials generated with ld1.x (V [Ar] 3d^3 4s^2, five valence electrons, no 3s3p semicore states; O [He] 2s^2 2p^4); plane-wave cut-off 60 Ry (charge density 240 Ry); 4 × 4 × 4 Γ-centered k-point mesh; Gaussian smearing 0.02 Ry; spin-unpolarized; crystal symmetry not used; SCF convergence 10^{-10} Ry and DFPT threshold 10^{-14}; Γ point only; crystal acoustic sum rule. The structure is the 12-atom M1 cell with the measured cold-M1 lattice (a = 5.7517, b = 4.5378, c = 5.3825 Å, β = 122.646°) and the refined V and O coordinates of the transforming M1 phase, averaged over 0.5–4 ps at 8.0 mJ cm^{-2}. It is not relaxed and the occupations are those of the ground state, so the photoexcitation enters only through the measured atomic positions. Two modes of this nonequilibrium geometry are unstable (5.2i and 4.1i THz) and are not shown. The 7.46-THz mode is assigned by its displacement character, not by the nearest DFPT frequency, to the longitudinal V–V chain mode, polarized along c_R. The most longitudinal DFPT mode between 6.5 and 8.5 THz lies at 8.28 THz in cold M1 and at 6.90 THz in the photoexcited structure (95% and 85% of the displacement along c_R); the fitted 7.46 THz falls between the two, as expected for a partly transformed lattice.

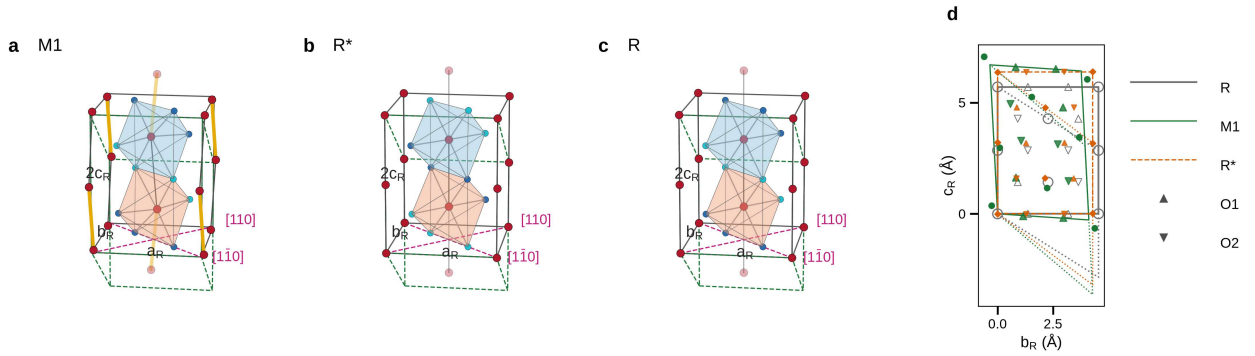
Supercells (Extended Data Fig. 6). The nodes λ = 0.85, 0.75, 0.625, 0.5, 0.375 and 0.25 are built on the refined R* at 3.57, 8.30, 18.31, 28.07, 49.95 and 79.30 ps (8.40 mJ cm^{-2}). The 16 chains form two sublattices of eight (corner and body center) whose zigzags point along perpendicular directions. The offset m = ¼ is the


a 13.64 mJ cm−2
b 11.22 mJ cm−2
c 8.40 mJ cm−2
d 6.90 mJ cm−2
e 6.16 mJ cm−2
f 5.00 mJ cm−2
g 4.52 mJ cm−2
h 4.29 mJ cm−2
(011)
(200)
(020)
(212)
(012)
(220)
(231)
(411)
(033)
(102)
(302)
(122)
(022)
(313)
(402)
(040)
(014)
OPP
Time (ps)

Extended Data Fig. 1 | Ultrafast electron diffraction and optical transmission at all eight fluences. a–h, 13.64, 11.22, 8.40, 6.90, 6.16, 5.00, 4.52 and 4.29 mJ cm^{-2} (Fig. 2a shows 11.22, 8.40, 6.90 and 4.29 mJ cm^{-2}). In each panel, the first 17 subpanels give the intensity of the indicated reflection (M1 indices), normalized to its value before time zero; red dots, measured; blue line, intensity computed from the refined structures, phase fractions and Debye–Waller factors of the model, including dynamical scattering. The y axis is shared along each row; dotted line, 1. Last subpanel (gray background; right axis): transmission change $\Delta T/T_0$ recorded simultaneously on the same film, measured (red dots) and model (blue line); dotted line, 0. Time axis logarithmic, 0.1–3000 ps.

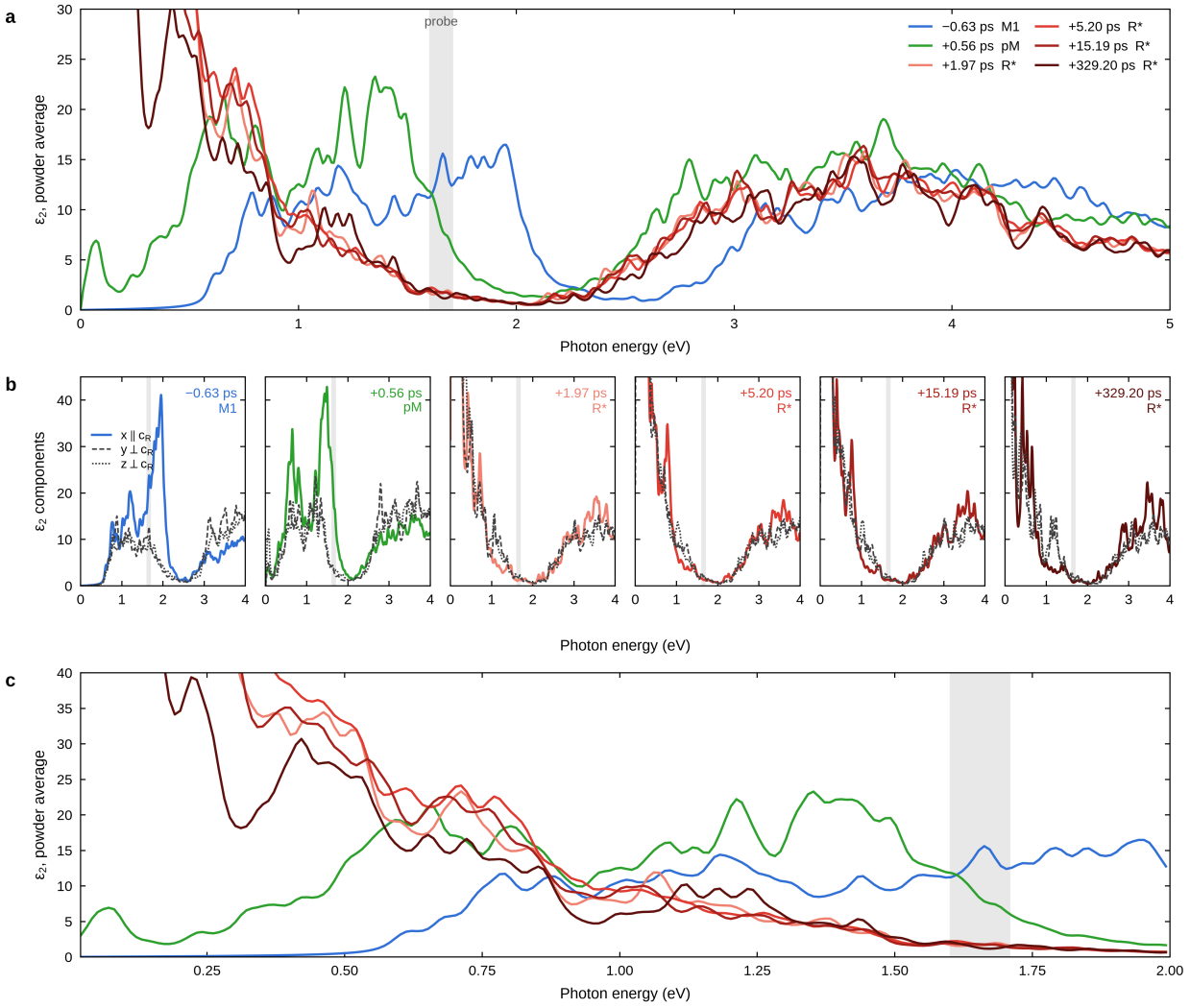


Extended Data Fig. 2 | Coherent A_g phonons from one joint fit of electron diffraction and optical pump–probe data. Frequencies of the three coherent A_g modes at 8.0 mJ cm^{-2} against the angle θ_{PP} between probe and pump polarization, from a single fit of the eleven traces of Fig. 2b: six diffraction channels (O1 and O2 displacements along the M1 axes a, b and c; 0.05–2.5 ps) and the optical transmission change at θ_{PP} = 15, 25, 47, 71 and 90° (0.05–0.70 ps), with three damped oscillators and the optical frequency law $f(\theta_{PP}) = f_0 - \beta \cos 2\theta_{PP}$ (441 points, 90 parameters, reduced χ^2 0.93; Methods). Diamonds, f_0 (diffraction), placed at 45° (dashed vertical line), where $\cos 2\theta_{PP} = 0$ (error bars ±1 s.d.). Circles, optical frequencies at the five measured angles from the fitted law. Shaded bands, β within $\Delta\chi^2 \leq 1$. $A_g(2)$: f_0 = 5.67 ± 0.08 THz, β = +0.06 THz (−0.08 to +0.21). $A_g(3)$: f_0 = 7.46 ± 0.08 THz, β = +0.10 THz (0.00 to +0.19). $A_g(1)$ (dashed line, open circles): f_0 = 4.43 ± 0.05 THz; angular law not determined (optical term decays within 67 fs). Dotted lines in the mode color, the DFPT zone-center (Γ) modes bracketing each fitted frequency; gray lines, all real DFPT Γ modes of the photoexcited structure (Methods).

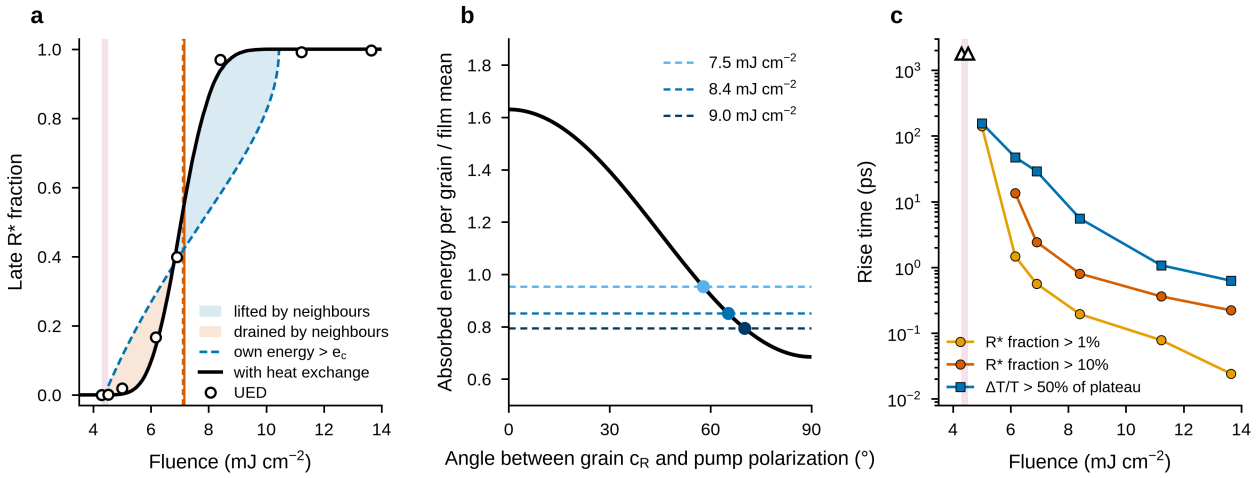


Extended Data Fig. 3 | M1, R* and R in the doubled rutile cell, with the two oxygen sites. **a**, M1: mean of the 7 refined structures before time zero (13.64 mJ cm^{-2}). **b**, R*: mean of the 5 refined R structures at t ≥ 1000 ps at the same fluence (R* fraction 0.997), in the rutile cell refined from the late diffraction peak positions. **c**, Ideal rutile R (u = 0.3001). Each box is the doubled rutile cell $(a_R, b_R, 2c_R)$, $a_R = b_{M1}$, $b_R = -(c_{M1} + a_{M1}/2)$, $c_R = -a_{M1}/2$; green dashed, the M1 cell. V, red; O1, dark blue; O2, cyan. Gold bonds, V–V < 2.75 Å; gray bonds, longer contacts; shaded, VO_6 octahedra of the body-center chain. Magenta dashed lines, [110] ∥ q(0$\bar{2}\bar{2}$) and [1$\bar{1}$0] ∥ q(033). M1: V–V 2.60/3.20 Å, V offset 0.173 Å perpendicular to c_R; O–V 1.86/1.89/2.03 Å (O1), 1.74/2.04/2.08 Å (O2). R*: V–V 2.86 and 2.88 Å, offset 0.001 Å; O–V 1.91/1.92/1.94 Å (O1), 1.92/1.94/1.94 Å (O2). R: O–V 1.92/1.92/1.93 Å. **d**, The monoclinic plane $(b_R, c_R) = (a_{M1}, c_{M1})$ viewed along a_R; strain relative to R magnified 20 times, atomic offsets from R doubled. Solid, the $(b_R, 2c_R)$ face; dotted, the M1 cell. Gray open symbols, R; green, M1; orange, R*. Circles and diamonds, V; up triangles, O1; down triangles, O2. Cell parameters (a_R, b_R, c_R; $\angle(b_R, c_R)$; a_{M1}, b_{M1}, c_{M1}; β_{M1}): M1 4.538, 4.532, 2.876 Å; 90.35°; 5.752, 4.538, 5.382 Å; 122.64°. R* 4.541, 4.541, 2.868 Å; 90°; 5.736, 4.541, 5.371 Å; 122.28°. R 4.553, 4.554, 2.851 Å; 90.00°; 5.702, 4.553, 5.373 Å; 122.05°. M1 and R* cells are refined from 7 diffraction peaks before time zero and at t ≥ 1000 ps; the R* cell is tetragonal by construction (Methods).

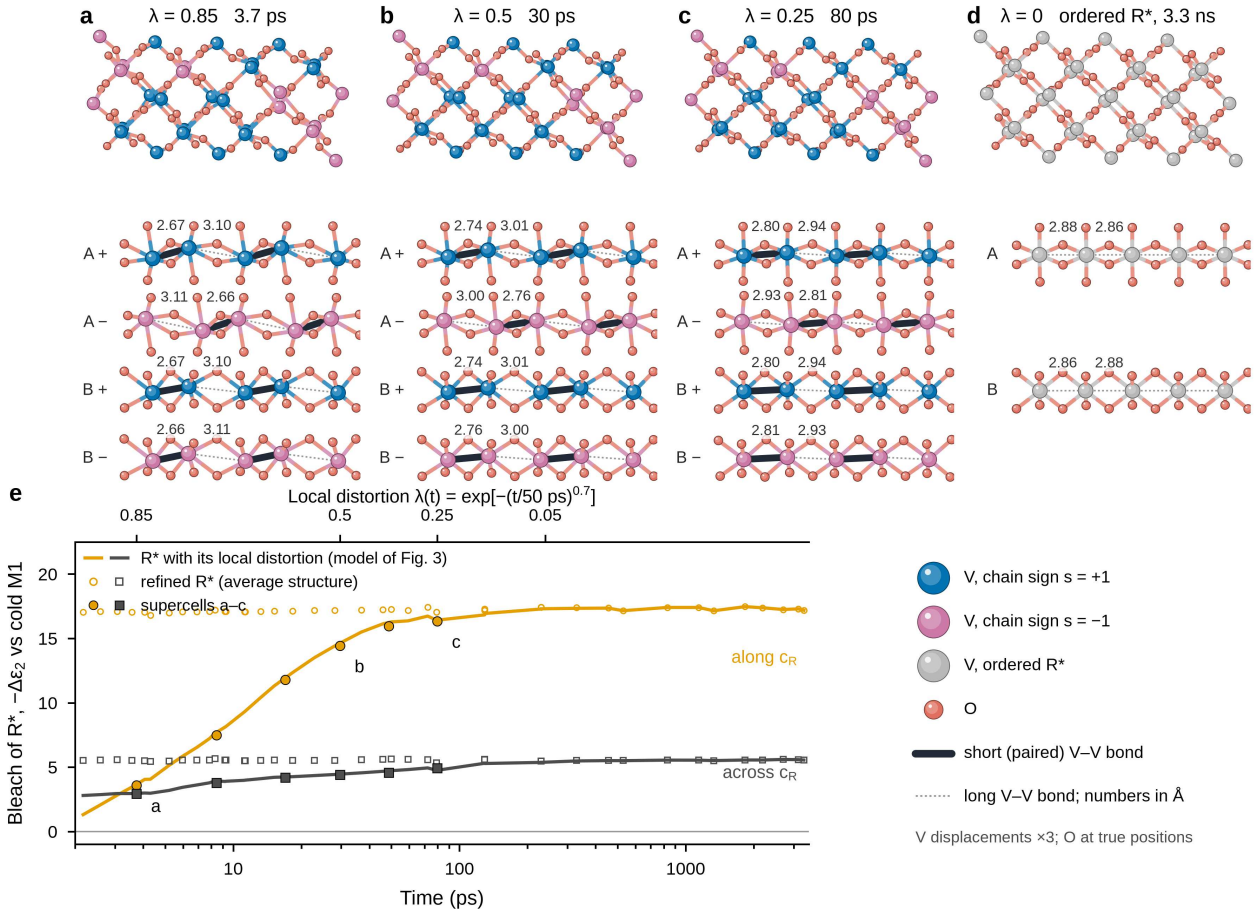
net M1-type pairing that the refined R* still carries (five of the eight chains of each sublattice are +), and the signs are arranged so that neighboring chains are as uncorrelated as a 16-chain cell allows. With a = 0.851 the chain-to-chain spread $a(1-m^2)^{1/2}\lambda$ is 0.824λ of the full M1 motif. Averaged over the eight tiles, every atom returns to its refined R* position to better than 10^{-6} Å, so the supercells give the refined R* intensity in every Bragg reflection; their static mean-square V displacement, λ² × 0.036 Å² (λ² × 0.016 Å² along the chains), does not exceed the measured V Debye–Waller excess of R*. The local distortion costs 219, 87 and 23 meV per V at λ = 0.85, 0.5 and 0.25 (DFT+U), so ordering is downhill. At λ = 1 the model uses a 48-atom (1 × 2 × 2) cell of the same local amplitude on the refined R* at 5.2 ps.



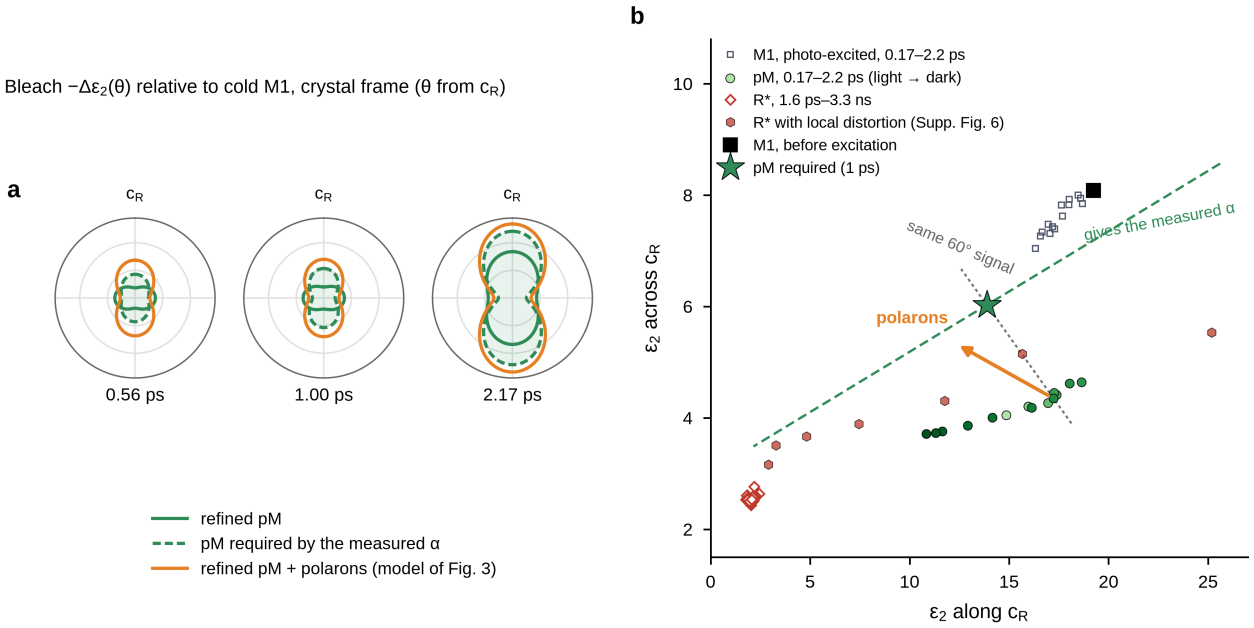
Extended Data Fig. 4 | Optical response of the refined average structures, computed as refined. DFT+U imaginary dielectric function ε_2 of the phase assigned at six delays at 8.4 mJ cm^{-2}: M1 at −0.63 ps (blue), pM at 0.56 ps (green) and R* at 1.97, 5.2, 15.2 and 329 ps (red, light to dark). Each calculation uses the 12-atom UED-refined cell drawn in Fig. 2c (refined lattice constants and V and O fractional coordinates; cell calibrated to bulk M1[32]), without relaxation, symmetrization or other adjustment. No supercell and none of the additions of the optical model (maturation, aging, polaron term, local distortion of R*) enter; the optical model reads pM at 0.30–1.00 ps with the oxygen trajectory regularized in time (Methods). **a**, Powder average $(\varepsilon_{2,x} + \varepsilon_{2,y} + \varepsilon_{2,z})/3$. **b**, Tensor components: x along a_{M1}, the V-chain direction ($\parallel c_{\mathrm{R}}$; colored), y and z perpendicular (gray dashed and dotted). **c**, Powder average below 2 eV. Gray band, the 725–775-nm DFT readout window. Read as in the optical model (750 nm, 50 nm FWHM, re-broadened to 0.20 eV), ε_2 along/across c_{R} is 19.2/8.1 for M1, 18.5/4.6 for pM, and 2.2/2.6, 2.3/2.6, 2.1/2.5 and 1.9/2.6 for R* at 1.97, 5.2, 15.2 and 329 ps. Spectra are drawn with the 0.05 eV broadening of the calculation; the low-energy rise in pM and R* is the intraband response of the metallic cells. Calculation: PBE+U, U = 3.5 eV on V 3d, 6 × 6 × 6 k-point mesh, independent-particle approximation, unscaled (Methods).



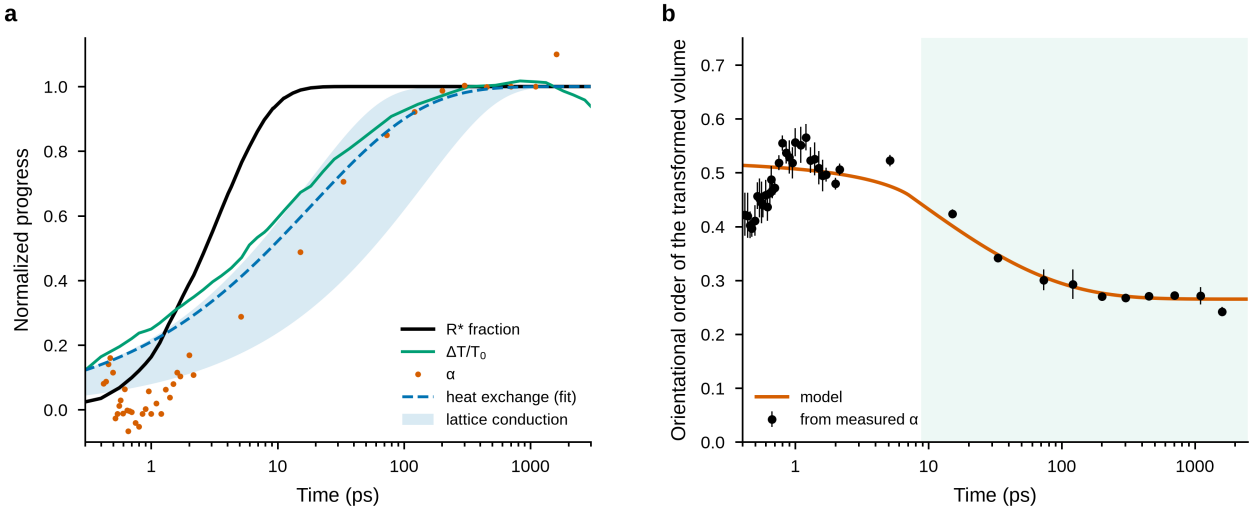
Extended Data Fig. 5 | A nonthermal onset F_c and a thermal threshold e_c, reached through heat exchange between grains, set the transformation window. a, Late R* fraction (mean over 1–3 ns) from UED at eight fluences (open circles). Dashed blue, grains whose own absorbed energy exceeds the threshold e_c = 7.15 mJ cm^{-2} (solid vertical line; fitted to the polar anisotropy, Fig. 3e), for absorption $a(\theta) = a_\perp + (a_\parallel - a_\perp)\cos^2\theta$ (θ, angle between c_R and the pump polarization; random 3-D orientations; $a_\parallel/a_\perp$ = 2.38 from DFT+U, not fitted; Methods). Black, with intergrain heat exchange; $1/k_0$ = 81 ps is the only parameter fitted to the late fractions. Orange shading, grains drained below e_c by colder neighbors (model 0.003, 0.14 and 0.43; measured 0.02, 0.17 and 0.40 at 5.00, 6.16 and 6.90 mJ cm^{-2}); blue shading, grains lifted above it by hotter neighbors (0.94; measured 0.97 at 8.40 mJ cm^{-2}). Dashed vertical line, F_{50} = 7.1 mJ cm^{-2}. Purple band, F_c = 4.40 mJ cm^{-2} (bracketed by 4.29 and 4.52). **b**, Absorbed energy relative to the film mean against θ (solid; before exchange), from 0.68 (θ = 90°) to 1.63 (θ = 0°). Dashed lines, e_c/F at 7.5, 8.4 and 9.0 mJ cm^{-2}; dots, crossing angles θ^* = 58°, 65° and 70°, below which 47%, 58% and 66% of grains exceed e_c on their own. **c**, Critical slowing down. Circles, time at which the R* fraction first exceeds 1% (yellow) and 10% (orange). Squares, last time ΔT/T (800 nm, same film) rises through 50% of its plateau. Open triangles, 4.29 and 4.52 mJ cm^{-2} (no ΔT/T rise exceeding 3% within 3 ns). From 13.64 to 5.00 mJ cm^{-2}, the 1% time grows from 0.024 to 140 ps and the rise time from 0.63 to 157 ps.



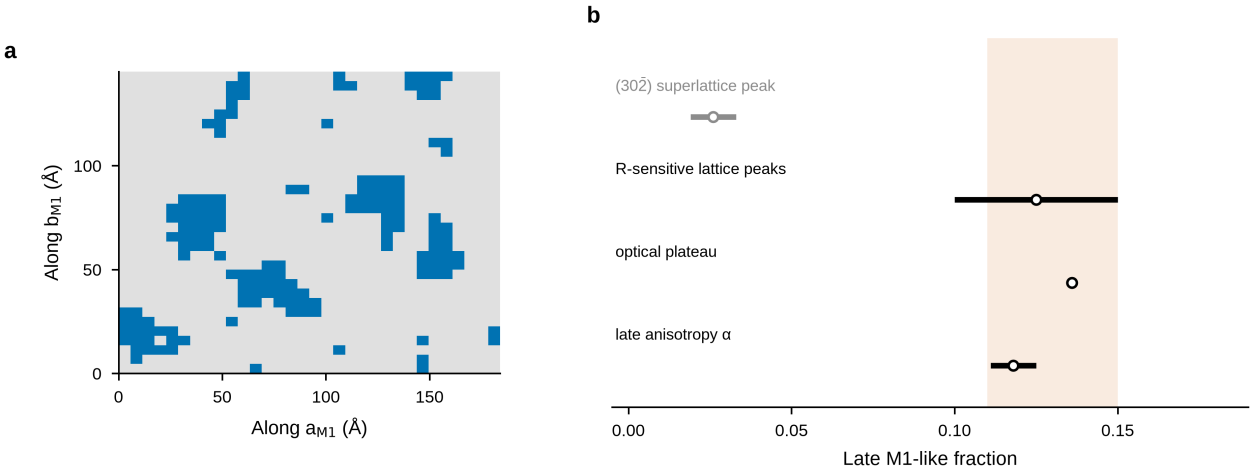
Extended Data Fig. 6 | R* forms with local M1-type chain distortions that are uncorrelated between chains, and these order on a 50-ps scale. Supercells (96 atoms, 16 V chains along c_R; 8.40 mJ cm^{-2}) built on the refined R*, whose chains carry a local M1-type distortion of amplitude λ and uncorrelated sign; they have the average structure of the refined R* and are the R* structures read by the model of Fig. 3c,d (construction in Methods). **a–d**, Cells at λ = 0.85 (3.7 ps), 0.5 (30 ps) and 0.25 (80 ps), and the refined R* at 3.3 ns (λ = 0); V displacements magnified 3 times. Top, the cell viewed 12° off c_R: V colored by chain sign (blue, s = +1, paired as cold M1; purple, s = −1; gray, ordered R*), O red; thick dark bonds, paired V–V bonds. Bottom, a + and a − chain of each sublattice with their O octahedra, two periods along c_R (horizontal); numbers, V–V distances (2.67/3.10, 2.74/3.01 and 2.80/2.94 Å at λ = 0.85, 0.5 and 0.25; 2.86/2.88 Å in ordered R*). **e**, Bleach of R* relative to cold M1, −Δε$_2$, along (orange) and across (gray) c_R (DFT+U, independent-particle approximation, crystal frame, 725–775-nm DFT readout window, without the global factor 0.65 of Methods). Lines, R* with its local distortion at λ(t), as read by the model; open symbols, refined R* alone; filled symbols, supercells **a–c**. Along/across, 3.6/2.9 at λ = 0.85; along, 14.4 at λ = 0.5 and 17.0 in ordered R* (5.5 across). Top axis, λ(t) = exp[−(t/50 ps)^0.7], selected by the 60° ΔT/T data (Fig. 3c). R* younger than ~2 ps is not shown.



Extended Data Fig. 7 | The early polar anisotropy needs the photodoped polarons; no refined structure supplies it. **a**, Bleach of pM relative to cold M1 in the crystal frame, $-\Delta\varepsilon_2(\theta) = -(\Delta\varepsilon_2\| \cos^2\theta + \Delta\varepsilon_2\perp \sin^2\theta)$, θ from c_R (up), at 0.56, 1.00 and 2.17 ps (DFT+U, independent-particle approximation, 725–775-nm DFT readout window, raw units; rings 5 and 10). Green solid, refined pM (1.9–2.0 along, 3.7 across at 0.56–1 ps). Green dashed and shaded, the pM required by the measured polar anisotropy, with the rest of the model of Fig. 3 and the isotropic absorption unchanged (along/across 4.3/2.5 at 0.56 ps, 5.4/2.1 at 1 ps, 12.1/2.5 at 2.17 ps). Orange, refined pM with the polaron term of the model (7.0/2.7 at 1 ps). **b**, Crystal-frame ε_2 along against across c_R (same calculation and units) of every structure the model uses at 8.40 mJ cm^{-2}: cold M1 (black square), refined photoexcited M1 (open squares) and pM (circles, light to dark) at 0.17–2.2 ps, refined R* at 1.6 ps–3.3 ns (open diamonds) and R* with its local M1-type distortion (hexagons; Extended Data Fig. 6). At 1 ps, pM gives 17.2 along and 4.4 across (M1, 19.2 and 8.1). Green dashed, pM responses that give the measured α at 1 ps with the rest of the model unchanged; gray dotted, pM responses with the same isotropic absorption, i.e. the same 60° signal (Fig. 3c), as the refined pM. Star, the pM that both require (13.9 along, 6.0 across; 5.3–6.3 across over the measured α at 0.56–2.15 ps); refined structures that absorb 13.9 along absorb 3.8–4.0 across. Orange arrow, the polaron term from pM at 1 ps (‖ −5, hole-polaron bleach of the V–V dimer transition; ⊥ +1, π* electron absorption), ending 0.3 from the measured-α line.



Extended Data Fig. 8 | Heat exchange between grains continues for hundreds of picoseconds after the conversion. **a**, Normalized progress of the R* fraction (UED, 8.4 mJ cm^{-2}; black), the transmission change $\Delta T/T_0$ at a pump–probe angle of 60° (8.4 mJ cm^{-2}; green) and the polar anisotropy α (8.6 mJ cm^{-2}; orange dots), with the completed fraction of intergrain heat exchange in the model of Fig. 3 (dashed; mean time 38 ps, half exchange 8.8 ps) and for lattice conduction (blue band). The band is $1-\varphi_\ell(t)$ for a checkerboard of cubic grains of edge ℓ in perfect thermal contact, $\varphi_\ell(t) = \left[(8/\pi^2)\sum_n \exp(-(2n+1)^2\pi^2 D_{\mathrm{th}} t/\ell^2)/(2n+1)^2\right]^3$, with no free shape parameter[37]; slow edge, ℓ = 90 nm and D_{th} = 1.2 × 10^{-6} m^2 s^{-1}; fast edge, ℓ = 40 nm and D_{th} = 2.0 × 10^{-6} m^2 s^{-1}. Grain sizes from STEM imaging of these films; $D_{\mathrm{th}} = \kappa/C$ from published conductivity and heat capacity (Methods). The model kernel is fitted to the polar anisotropy at six fluences, not to the band (e_c = 7.15 mJ cm^{-2}, response exponent 0.99, time 18.6 ps, stretch 0.49), and lies inside the band from 0.1 ps to 2 ns. **b**, Orientational order of the transformed volume at 8.6 mJ cm^{-2}, inferred from the measured α with the crystallite anisotropy D(t) of the model (black dots) and from the model of Fig. 3 (line; same exchange law). The point at 5.1 ps lies above the line, where the model's α exceeds the measured value (Fig. 3d). Shaded region (t > 8.8 ps), heat exchange more than half complete.



Extended Data Fig. 9 | A hidden M1-like remnant at 8.4 mJ cm⁻²: seen by the R-sensitive lattice peaks, missed by the superlattice peaks. Superlattice peaks, such as (30$\bar{2}$) and (31$\bar{3}$) (M1 indices), exist only in M1 and change sign between the two antiphase M1 variants; they measure the volume of long-range, coherent M1 order. R-sensitive lattice peaks, allowed in both M1 and R*, have the same structure factor for both variants and measure the volume carrying the local M1 arrangement, whatever its correlation length. **a**, Real-space model of the remnant used in the kinematic diffraction simulation: one slice (c_{M1} = 0) through a film of 32 × 32 × 32 M1 cells (184 × 145 Å shown). Gray, R*; blue, cells that keep M1-like order (13% of the volume, one M1 variant), reached last by isotropic R* growth from random nuclei (mean spacing 4 cells; pocket mean chord 13 Å). Simulated readout: 0.13–0.14 on the R-sensitive lattice peaks free of superlattice reflections, (0$\bar{1}$1), (200), (020), (2$\bar{1}$2), (01$\bar{2}$), (2$\bar{2}$0) and (23$\bar{1}$)+(202), but 0.01–0.02 on (30$\bar{2}$); pockets of mixed antiphase variants up to 23 Å read ≈ 0 on (30$\bar{2}$) and 0.12–0.14 on the R-sensitive peaks. **b**, Late-time (t ≥ 1 ns) M1-like fraction from four observables: (30$\bar{2}$) intensity relative to M1 before excitation (UED; gray); 14 R-sensitive lattice peaks at 8.4 mJ cm⁻², fitted as a mixture of the pattern at 11.2 mJ cm⁻² (no remnant) and that of M1 before excitation (UED); the optical plateau per converted volume relative to 11.2 mJ cm⁻² (optical pump–probe); and the late anisotropy α if the remnant sits in one orientation class (optical pump–probe). Bars, ranges; circles, central values. Three observables agree on about 13% (shaded, 11–15%); the superlattice peak reads 3%.